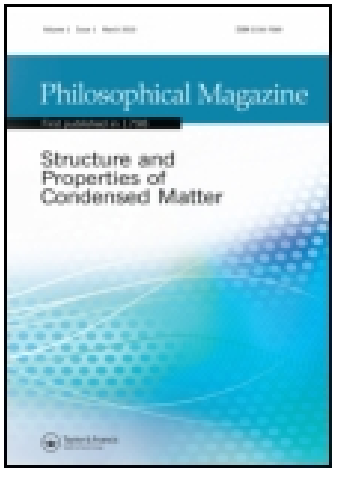

Philosophical Magazine
Publication details, including instructions for authors and subscription information:
http://www.tandfonline.com/loi/tphm20

Multiscale crystal defect dynamics: a dual-lattice process zone model

Shaofan Li[a], Bo Ren[a] & Hiroyuki Minaki[b]
[a] Department of Civil and Environmental Engineering, The University of California, Berkeley, CA 94720, USA.
[b] Department of Mechanical Engineering, The University of California, Berkeley, CA 94720, USA.
Published online: 07 Apr 2014.

To cite this article: Shaofan Li, Bo Ren & Hiroyuki Minaki (2014) Multiscale crystal defect dynamics: a dual-lattice process zone model, Philosophical Magazine, 94:13, 1414-1450, DOI: 10.1080/14786435.2014.887859

To link to this article: http://dx.doi.org/10.1080/14786435.2014.887859

Philosophical Magazine, 2014
Vol. 94, No. 13, 1414–1450, http://dx.doi.org/10.1080/14786435.2014.887859

Multiscale crystal defect dynamics: a dual-lattice process zone model

Shaofan Li[a]*, Bo Ren[a] and Hiroyuki Minaki[b]

[a]*Department of Civil and Environmental Engineering, The University of California, Berkeley, CA 94720, USA;* [b]*Department of Mechanical Engineering, The University of California, Berkeley, CA 94720, USA*

(*Received 26 August 2013; accepted 21 January 2014*)

In this work, we present the theoretical and computational formulations of a multiscale crystal defect dynamics (MCDD) for the simulation of crystal defects at small scales. The main novelties of the proposed MCDD are: (1) We use the dual-lattice tessellation to construct a dual-lattice process zone model that can represent different types of crystal defects in a single crystal; (2) We adopt a fourth-order (four scales) hierarchical strain gradient theory to model constitutive behaviours of various defect process zones, in which the atomistic-informed higher order Cauchy–Born rule is employed, and (3) We employ the Barycentric finite element technique to construct finite element shape functions for polygonal and polyhedral process zone elements. The proposed MCDD method provides an efficient and viable alternative for both molecular dynamics and dislocation dynamics in simulations of defect evolutions such as void growth, dislocation nucleation, and fracture. In particular, MCDD offers a mesoscale description for dynamic lattice microstructure, defect microstructure, and their interactions. The method offers a possible solution for studying nanoscale and mesoscale crystalline plasticity.

Keywords: defect mechanics; dislocation dynamics; embedded atom method; finite element method; mesoscale plasticity; multiscale simulation

1. Introduction

Crystal defects such as voids, dislocations and cracks are intrinsically multiscale objects, and they are present in massive quantities in engineering crystalline materials. The statistical behaviours of aggregated defects determine macroscale material behaviours, which are strongly influenced by interactions between crystal microstructure and defects. This makes the prediction on material failure as one of the most difficult and elusive problems in materials science as well as in condensed matter physics. For example, even though crystal lattice dislocation was identified as the basic mechanism of metal plasticity as early as 1930s, our understanding of metal plasticity initiation and subsequent plastic deformation are still limited and incomplete. Today, nanoscale plasticity has become a focal point for nanoscale material design and manufacture. A critical issue in nanoscale plasticity is to find the precise atomistic origin of crystalline plasticity, and a significant amount of research works have been focusing on using first principle-based approach (e.g. [52]) to

*Corresponding author. Email: shaofan@berkeley.edu

link the structure and motion of dislocation loops with material properties. However, even with the state-of-the-art computing technology, the first principle-based approach is still hinged by limited computing resource. This difficulty may persist even if we had unlimited computational power, because without an adequate multiscale analysis tool we may not be able to extrapolate useful statistical information from massive data at microscale to gain insights on the complex multiscale physical phenomenon. Alternatively, dislocation dynamics (DD), e.g. [2,8,17,23,34], is another popular approach that attempts to characterize behaviours of aggregated dislocation ensembles at mesoscale. However, DD also suffers a number of shortcomings. For example, the theoretical framework of DD is based on isotropic linear elasticity theory, which ignores the non-linear and anisotropic nature of crystal lattice deformation; and moreover, the dislocation core cut-off radius r_0 used in DD is a user-chosen constant, and thus it may lead to inconsistency in dislocation energy calculations. In fact, in DD, the ratio of dislocation energy vs. dislocation core size is of the order of $\sim\log(R/r_0)$, which diverges when the length scale approaches the core size.

Towards a multiscale material modelling paradigm, many multiscale computational models have been proposed in the literature in the past two decades, and the most notable examples of active multiscale methods include: coupling length scale method e.g. [1]; quasi-continuum method e.g. [40,56]; virtual internal bond model e.g. [22]; bridging scale method e.g. [47,60]; concurrent atomistic-continuum method e.g. [10,11,62,63]; and several molecular dynamics to continuum methods, e.g. [12–14,28,33]. In particular, some of these methods and others have been used in mutliscale material modelling and design, e.g. [41–43].

To further advance multiscale material modelling, the present authors have developed an atomistic-informed multiscale process zone model in a series of publications e.g. [35, 36,38,46,49,66], which adopts the philosophy of fracture process zone (FPZ) approach in non-linear fracture theory. Here, we want to stress the distinction between the process zone model and the cohesive zone model: We refer the process zone as a finite size bulk volume *interphase* zone that is a defect embedded space, or simply the volumetric presence of the defect, whereas the cohesive zone is traditionally referred to as a zero volume interface zone with prescribed surface cohesive law. Moreover, we note that there are also major differences between the concept of FPZ and the dual-lattice process zone (DLPZ) proposed in this work. In fracture mechanics, ductile materials FPZ is a small, changing, but finite size yielding zone where strain hardening dominates over strain softening. Because of the existence of FPZ, crack tip can be easily distinguished from undamaged material, and inside the FPZ there are abundant dislocations and other microscale defects. In the proposed dual-lattice process zone model, the process zone is a finite volume region that can host defect aggregates or it may be simply regarded as a fine scale representation of potential defect zone in contrast to macroscale FPZ that has changing morphology due the magnitude and history of the external loadings. In this work, we apply the DLPZ approach to systematically study defect dynamics in crystalline materials. Here the term defect is referred to the disorder or damage state of lattice structure, which includes voids and vacancies, dislocations and disclinations, lattice slip, grain boundaries and twin boundaries, and cracks. In passing, we note that a similar idea of atomistic-informed lattice dynamic finite element analysis (FEA) has been pursued by [37], except that the main technical gradient of that work is the application of a modified Cauchy–Born rule in conventional FEA.

This paper is organized into seven sections: in Section 2 we shall first discuss the concept of DLPZ model. In Section 3, we discuss how to construct the DLPZ tessellation

for both BCC and FCC lattices, and how to model the various defects by using different order process zones; in Section 4, we shall discuss an atomistic-informed strain gradient constitutive theory for different order process zones; in Section 5, we discuss the finite element formulation of multiscale crystal defect dynamics (MCDD), and the computer implementation of MCDD finite element formulation. To demonstrate its feasibility and validity, we present two numerical examples in Section 6. Finally, in Section 7, we summarize the present work, and comment on the various perspectives of MCDD.

2. DLPZ model

To study the overall material behaviours dictated by the aggregated defect motions has been a longstanding challenge of condensed matter physics and materials science. The first-principle approach is to examine the deformed configuration of spatial atom arrangement by using molecular dynamics simulations as mentioned in Section 1. Realizing that there are only a few types of lattice defects in crystalline solids, mainly dislocations, voids, disclinations, lattice slip and cracks, a conventional approach is to use lower dimension geometric models, such as surfaces (2D), line segments (1D) and vertex or point (0D) to present the defects in crystalline solids, and study their evolutions. A very popular example of such approach is the discrete DD e.g. [17,23]. A recent example is the discrete mechanics of crystal lattice developed by [3], in which the defects are again treated as lower dimensional objects of lattice complex; for example, the void is idealized as the point defect (0-cell), dislocation is idealized as the line defect (1-cell) and crystal slip is idealized as surface defect (2-cell), which are the prototype defect models that are commonly adopted in standard dislocation mechanics, e.g. [26]. On the other hand, the lower dimensional idealization or modelling of defects has some inherent shortcomings, because it is hardly the physical reality of defect mechanics. As it is well known that all physical defects occupy three-dimensional space, dislocations have complex three-dimensional core structures, e.g. [9], and most of the point defects are finite volume voids and cavities instead of a single point. Treating defects as lower dimensional objects often results in failure to predict some essential physical features of defect mechanics, because of its dimensionality limitation. Mathematically, the lower dimensional defect model often requires a regularization provision to justify its mathematical existence and physical sensibility; for instance, the well-known Peierls–Nabarro model for dislocations in linear elasticity media. Because of its dimension limitation, the lower dimensional defect model usually does not have scale length, and thus fails to provide statistical insights and relevance to the original physical problems. Instead of using a low-dimensional geometric entity to model the defect, in the present study, we propose to use the extended 3D geometric entity, i.e. dual-lattice tiling, to represent the defect. We refer the extended geometric entity as the dual-lattice process zone in the spirit of the process zone in fracture mechanics. In this section, we first discuss the concept of the dual-lattice process zone tiling, which was evolved from an atomistic-informed interphase zone model developed by the present authors in a series of publications, e.g. [24,35,36,38,49].

2.1. *Dual lattice and dual-lattice tessellation*

The conventional approach on partition of a lattice space is using atom sites as vertices and connecting them with a topological structure that occupies the whole lattice space. The

most common examples of lattice structures are: the body centre cubic (BCC) lattice, the face-centre cubic (FCC) lattice and the hexagonal close-packed (HCP) lattice, in which each vertex of the crystal lattice complex is an atom site. In crystallography, there is a unique dual lattice for every lattice structure, and the vertex of the dual lattice is not an atom site (see Figure 1). One can see that each atom sits at the centre of the so-called Voronoi cell, and the corresponding dual-lattice partition is also called the Voronoi–Dirichlet tessellation. If the Voronoi cell is convex, it is also called Voronoi–Dirichlet polyhedron (VDP). Each vertex of the dual lattice is a centre of a local VDP. The union of all local VDP will cover the entire lattice space.

To form a DLPZ solid, we first keep all the atom sites (the centre of Voronoi cell) fixed and scale down all local VDP; by doing so the union of all scaled local VDP will not be able to cover the whole lattice space, because the two adjacent VDP will not be in contact. Then, we connect all scaled VDPs with different convex polyhedra to fill the gap among them, and this process is called lattice tessellation, or lattice tiling. Note that in this paper the term "tiling" is used as a synonym of tessellation or mesh in both 2D and 3D.

A regular tiling places a fixed number of one type of regular convex polygon or polyhedron at each vertex of VDP, and in fact the original dual lattice is a regular tiling. However, once the original local VDPs are scaled down, one cannot use the regular tiling to partition the entire lattice. Under this scenario, we have to relax the symmetry requirement to allow two or more convex polyhedra to connect with each vertex but still requiring the same local symmetry pattern for each vertex. This is the so-called semi-regular tiling or the Archimedean tessellation.

To illustrate how to construct the DLPZ tessellation, we first consider an example of two-dimensional (2D) hexagonal lattice as shown in Figure 1. In Figure 1, the red points are atom positions and the solid lines are the representation of pair bonds, which form a 2D triangle lattice. The yellow points, on the other hand, are intersections or vertices of the

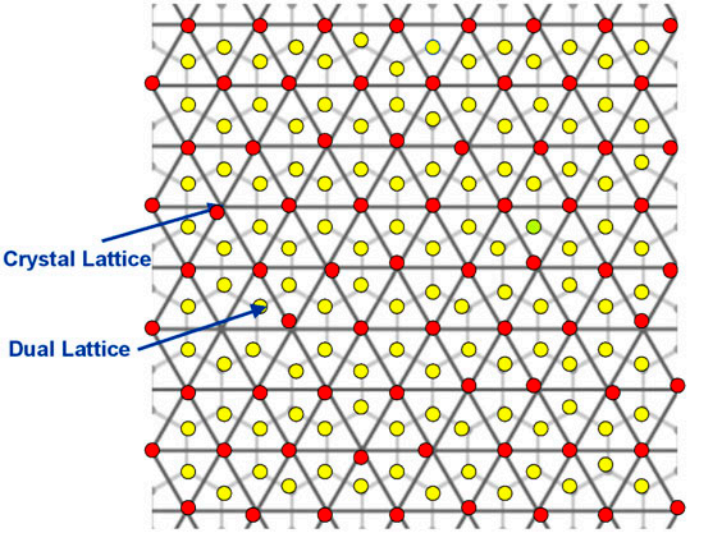

Figure 1. (colour online) Concept of lattice and dual lattice.

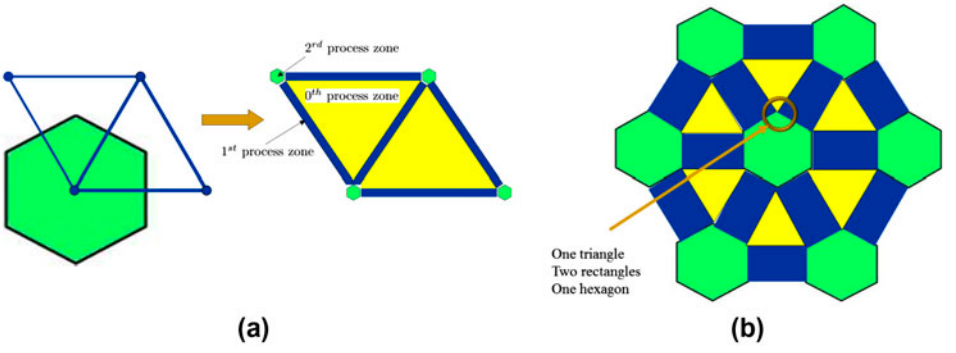

Figure 2. (colour online) Rhombihexadeltille: A dual-lattice process zone tiling.

dual lattice or reciprocal lattice, and the connecting lines among them forms the reciprocal hexagonal lattice.

In this example, we first scale down the Wigner–Seitz cell – the honeycomb element, and then fill the gap with the triangle elements that are laced together by rectangle elements. This dual-lattice tessellation process is called the rhombitrihexagonal tiling (Figure 2(b)). In geometry, the rhombitrihexagonal tiling (Figure 2(b)) is a semi-regular tiling of the Euclidean plane. There are one triangle, two squares and one hexagon on each vertex. It has the Schläfli symbol of $rr\{3, 6\}$, and it is called as a *rhombihexadeltille* or expanded hexagonal tiling [16], which is a special case of hexagonal cupola.

Here we refer the triangle tile as the bulk element, which may be labelled as the 0th-order process zone. The six-side honeycomb is the Wigner–Seitz cell of the triangle lattice, which we label as the second-order process zone, and finally we label the rectangle element as the first-order process zone, which serves as the interphase process zone between two triangle bulk crystal elements as shown in Figure 2(b). In Figure 3, we compare the dual-lattice process zone tessellation with the super DLPZ tessellation.

In summary, the key steps in the construction of a dual-lattice process zone tessellation are:

(1) Choose the whole set or a subset of the atoms that form a lattice or a supper lattice of the same symmetry and,
(2) Shrink the size of the corresponding Wigner–Seitz cell or VDP, and choose it as the highest order process zone element;
(3) Connect facets and edges of the resized Wigner–Seitz cells with a set of hierarchical polyhedra (in 3D) or polygons (2D) that are the lower order process zone elements;
(4) Use the bulk crystal elements (0th-order process zone) to connect vertices the of the Wigner–Seitz cells or VDPs and fill the empty gap in the entire lattice space.

We note that the study of lattice tessellation has a long history, and it has accumulated a large body of literature, e.g. [7,19,21,25,31,32] just to mention a few. Most of these works use the group theory to study the tessellation or tiling symmetric arrangements of spatially distributed atoms in crystals, and classify the lattice or dual-lattice complexes. Adopting a computational approach rather than mathematical proof, the present authors prefer to use an intuitive engineering approach that relies on pictorial reasoning to reveal the intriguing

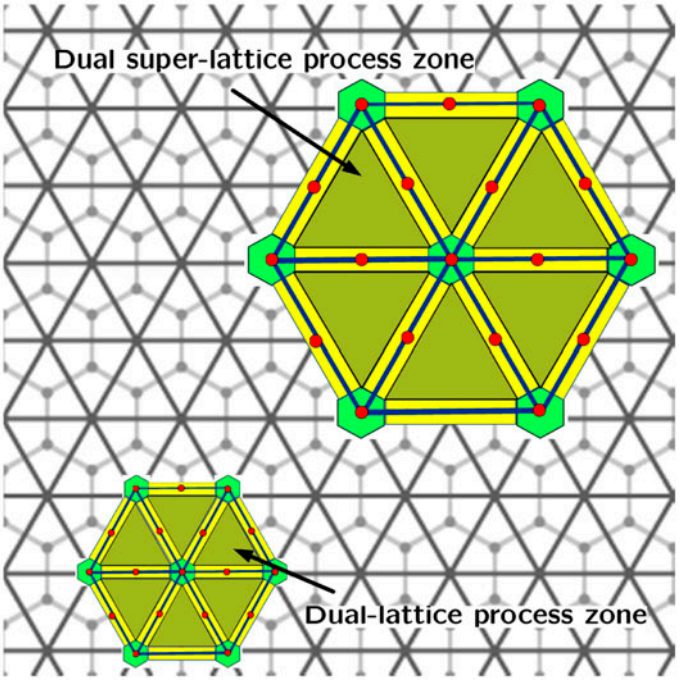

Figure 3. (colour online) Various dual-process zone tesellations: original DLPZ and Super-lattice DLPZ.

geometric topology relation of crystallography tiling, while other researchers may prefer to use algebraic and differential topology concepts and equations such as homology to aid their presentation e.g. [6,20]; and we defer the discussion of mathematical theorems and proofs to a separated exposition.

2.2. *Basic assumptions of MCDD*

Since our objective is to predict material failure at mesoscale, a central issue is: *what is the essential microstructure of defects at mesoscale?* For crystalline solids, the defect microstructure is often associated with the geometric configuration of defects, such as voids and cavities, dislocations, persistent slip bands, grain boundaries, twin boundaries, stacking faults and microcracks, etc. Based on experimental observation, we adopt the following kinematic and constitutive assumptions in the MCDD model:

(1) The deformation inside the bulk crystal element is uniform and homogeneous, whereas all the non-linear and non-uniform deformations are confined inside the process elements, and the order of non-linearity increases with the order of the process zone;
(2) Bulk crystal elements are modelled by the first-order Cauchy–Born rule, and the dual-lattice process zone elements are modelled by the higher order Cauchy–Born rules;

(3) Material failure is not defined solely as cleavage surface or interface separation, but it is due to the degradation of general bonding state including debonding and sliding.

It may be noted that traditionally the material strength was considered as the critical thermodynamics state of the bulk material, and the use of surface cohesion as the only measure of material strength became the dominant and popular theory only after 1960s. In fact, the kinematic assumption mentioned above is a reminiscence of the basic assumption of classical crystal plasticity [58], which has been widely accepted and recognized as the foundation of crystal plasticity model for polycrystalline solids. Similar kinematics assumptions have also been adopted in some other approaches, e.g. the Peierls–Nabarro model [34,45,48], in which the stacking fault cohesive zone is a finite width volume that can accommodate the finite size dislocation core, and the material inside the finite width cohesive zone is modelled as a special non-linear elastic medium, whereas outside the finite width cohesive zone, the material is modelled as linear elastic medium. The philosophy of MCDD is fundamentally different from that of conventional lattice dynamics or lattice defect mechanics. Recognizing the existence of various core structures for various types of defects, we model the potential defect zone as a three-dimensional finite size object using the DLPZs: we model the void as a Wigner–Seitz cell-shaped cavity; we model the slip plane as a finite width interphase layer; and we model the dislocation line as a thin prism with finite cross-section. By doing so, we specify geometric microstructures for defects. For example, the junction of dislocation lines automatically become a tiny finite volume polytope.

In order to maximize computational efficiency, MCDD may be implemented in a super dual-lattice process zone tessellation. The super dual-lattice process zone model reduces many degrees of freedom in computations by introducing internal kinematic constraints, and it thus has the advantage of continuum approach. Since we model the process zone as "a defect-prone zone", the DLPZ at atomistic scale is obviously the most accurate process zone model, because the defect can evolve in any possible atom site along all the possible directions, whereas for the pre-selected super dual-lattice defect process zone, it is only an approximation of the real lattice structure, because of the reduction of degrees of freedom due to the internal kinematics and geometric constraints. However, one can always refine MCDD finite element mesh to achieve atomistic resolution. The meaning of *multiscale* in the term of MCDD is twofold: the first is that for a give process zone tessellation there are four different scales of process zones, and the second is that MCDD has the scaling or switching ability of transcending from one length scale to another length scale through mesh refinement and adaptivity. For macroscale engineering applications, we may be able to use a coarse finite element mesh to obtain achievable and meaningful results with reasonable computation resource.

3. Dual-lattice tiling for BCC and FCC crystals

In this section, we first illustrate that it is possible and feasible to create a three-dimensional dual-lattice process tessellation for realistic crystalline solids, and that the DLPZ tessellation is a perfect cover of the entire crystal space. In specific, we shall construct the DLPZ tessellation for two most common crystal structures: (a) the body-centred cubic (BCC) crystal, and (b) the face-centred cubic (FCC) crystal.

3.1. *BCC dual-lattice process zone tessellation*

For a given crystal lattice, the construction of a dual-lattice process zone tessellation that can partition the entire lattice space is not unique, and it is not trivial either. To start, the first thing that we have to do is construct a Voronoi cell for each representative atom by using the so-called Voronoi–Dirichlet Partitioning technique to partition the lattice space around the chosen atom site by placing planes normal to line segment between two neighbouring atoms of the lattice complex at midpoints of the line segment. This will form a convex polyhedron around the central atom site, which we call as a Voronoi–Dirichelt Polyhedron (VDP). The subtle part of the Voronoi–Dirichlet partition is how to select the neighbouring atom sites to form VDP. With different choices of neighbouring atoms, the shape of the VDP will be different. For the BCC lattice, if we choose the neighbouring points by including its all eight nearest neighbour atoms, and additional six second nearest neighbour atoms, the Dirichlet partition should create a truncated octahedron, which is a special VDP that is called the Wigner–Seitz cell of the dual-lattice BCC complex, i.e. the unit cell of the reciprocal space (dual lattice). In passing, we note that the dual of the truncated octahedron is a rhombic dodecahedron, which is a BCC unit cell in the original lattice space (not dual-lattice space) as shown in Figure 4. If we choose more neighbouring atoms for a given centre atom, the shape of the dual-lattice VDP will change.

We now illustrate how to construct a 3D BCC dual-lattice process zone tessellation. To begin with, we first construct a special VDP, i.e. the Wigner–Seitz cell, for each selected atoms, and their union will form a perfect cover for the entire lattice space. This is true for both the original lattice as well as super lattices if the super Wigner–Seitz cell is used. Note that in the rest of the paper we always label VDP and its scaled derivatives as the highest order of the process zone – the third-order process zone.

Note that the Voronoi–Dirichlet partition is not the dual-lattice process zone tessellation. If we do not scale VDP or the Wigner–Seitz cell after the Voronoi–Dirichlet partition, all other lower order process zones including the bulk crystal elements will be in their degenerate states, and they are not live 3D objects, because the whole lattice space is partitioned by the third-order process zone only. To form a dual-lattice process zone tessellation with non-degenerate process zones, we need to scale down the size of VDP or the Wigner–Seitz

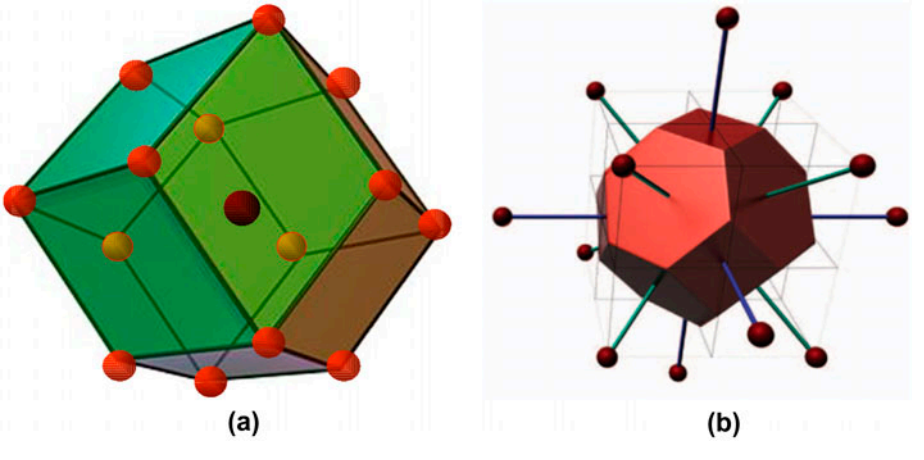

Figure 4. (colour online) (a) A BCC unit cell, and (b) A BCC Wigner–Seitz cell.

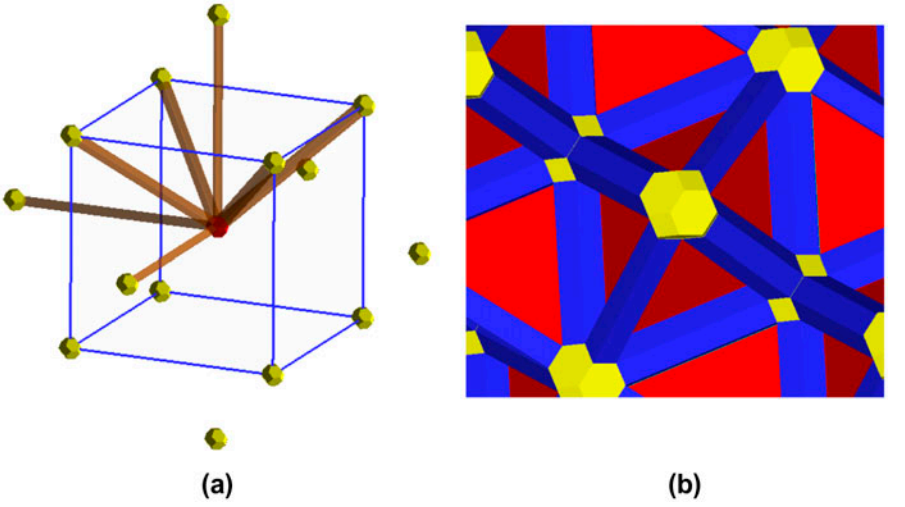

Figure 5. (colour online) (a) One third-order process zone and 14 second-order process zones (only shown seven of them), and (b) BCC third-order process zone and the second-order process zones in the bulk crystal.

cell, so that there will be open space among different Wigner–Seitz cells, or VDPs, which can then be filled by different order process zones. In specific, for BCC dual-lattice tessellation, there will be eight hexagonal prism elements and six square prism elements (Figure 5(a)) connecting to the 14 facets of the truncated octahedron and 36 thin plate elements connecting to the 36 edges of the octahedron (see Figure 6(a)–(f)), and 24 tetrahedron bulk crystal elements connecting to the 24 vertices of the octahedron (see Figure 6(g)–(l)).

Together with bulk crystal elements, the process zone elements can fill the entire lattice space perfectly. In summary, in a the BCC dual-lattice unit, there are: (I) one third-order process zone element that is the scaled Wigner–Seitz cell, or VDP; (II) 14 second-order process zone elements, among them eight are hexagonal prism process zone elements and six are square prism process zone elements; (III) 36 first-order process zone elements, which are planar stacking fault elements that may represent the six distinct slip planes as shown in Figure 6(a)–(f), and (IV) $6 \times 8 \times \frac{1}{2} = 24$ tetrahedral bulk elements (0th-order process zone) as shown in Figure 6(g)–(l). The above counting on the number of bulk crystal element is based on the fact that there are eight nearest neighbours in a BCC super lattice cell, and each nearest neighbour will form sic tetrahedral tiles; however, in each of this tetrahedral, one node is from the second neighbour, one node is the centre node and the rest two nodes are from the eight first neighbours; therefore, a factor 1/2 should be taken into account in tetrahedron counting.

Once again we note that to build a super lattice or super dual lattice, we only choose a subset of atoms in BCC lattice as the representative atoms, which retain the symmetry of the original BCC lattice. The term "super-lattice" in this paper is defined as a lattice with the exact same symmetry of the original lattice but having a larger lattice constant (na, $n > 1$). The super lattice VDP will have the same shape as that of the original VDP. The scaled VDP is referred to shrink the size of VDP proportionally for any (super) lattice desired, including the original dual lattice. A scaled super lattice VDP may contain many real atoms but just one representative atom.

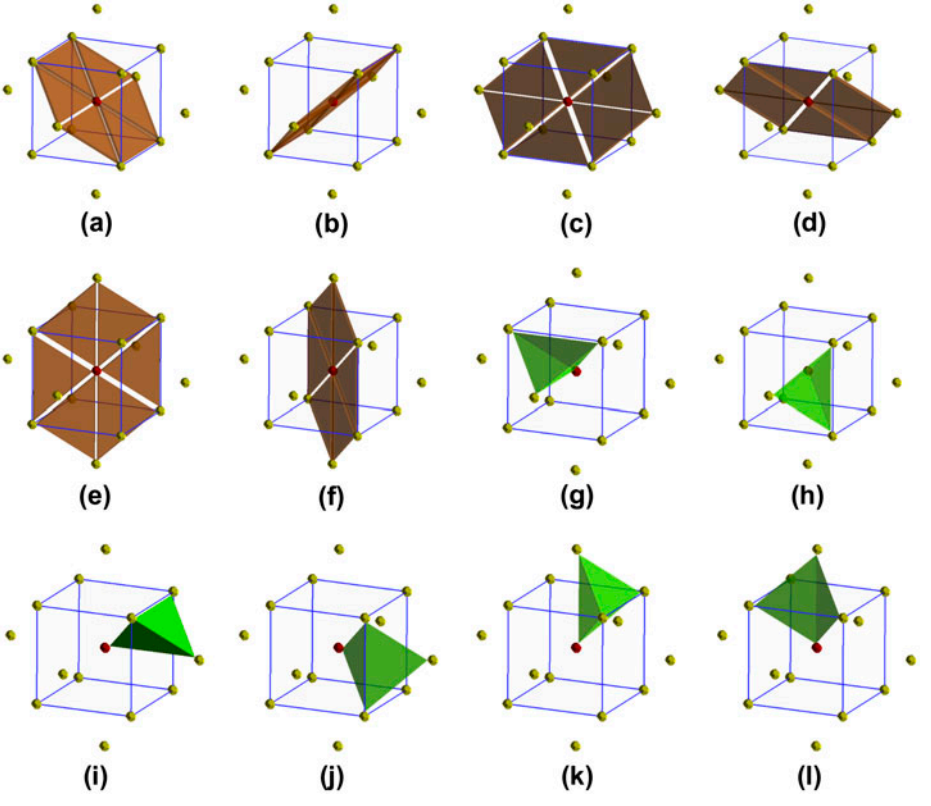

Figure 6. (colour online) There are six slip planes and 36 first-order process zone elements ((a)–(f)); and $6 \times 8 \times \frac{1}{2} = 24$ bulk tetrahedron elements ((g)–(l)) in a minimum BCC super dual-lattice unit cell.

Remark 3.1 Even though the MCDD approach is fundamentally different from that of the discrete mechanics of crystal lattice [3], the two can be related by an imaginary geometric scaling, and the original lattice complex is the scaling limit of MCDD dual-lattice process zone tessellation. In specific, after the scaling, the original lattice complex 0-cell "becomes" a finite volume tetradecahedron, or more precisely a truncated octahedron; some of the BCC lattice 1-cells (connecting to the first neighbours) "become" hexagonal prisms, and others (connecting to the second nearest neighbours) will "become" square prisms; the BCC lattice complex 2-cell maps to a finite thickness stacking fault process zone, and finally, the 3-cells will be mapped to the Wigner–Seitz elements, i.e. the truncated octahedron.

As mentioned above, to form a seamless process zone tessellation, each of the 14 prism process zone elements (second order) connect to one surface of 14 facets of the truncated octahedron (third-order process zone); each of the 36 first-order interphase stacking fault elements connect to one edge of 36 edges of the truncated octahedron, and finally each of the 24 bulk tetrahedron elements connect to one vertex of 24 vortices of the truncated octahedron (third-order process zone). This algebraic structure is manifested by the well-known Euler's polyhedron formula in algebraic topology as

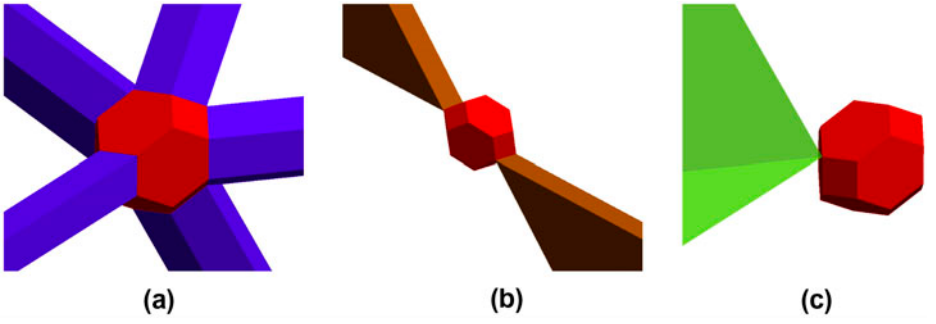

Figure 7. (colour online) Detailed connections between different order process zones in a BCC dual-lattice tessellation.

$$V - E + F = 2, \quad \text{in BCC DLPZ} :\Rightarrow \quad 24 - 36 + 14 = 2\,!$$

Figure 7 shows the detailed connections between the truncated octahedron element in the centre and the rest of the lower order process zone elements. For each vertex of the truncated octahedron, it is adjacent with one rectangle prime element, two hexagonal prime elements, three thin plate elements and one tetrahedron element.

3.2. *FCC DLPZ tessellation*

We now show how to construct a FCC dual-lattice process zone tessellation. Different from BCC DLPZ tessellation shown above, we consider a representative atom with its the nearest neighbours only, and then construct the corresponding Voronoi–Dirichlet polygon (VDP). For a representative atom in FCC lattice, its nearest neighbour VDP is a rhombic dodecahedron as shown in Figure 8(b), and its dual is a cuboctahedron cell (see Figure 8(a)). This particular VDP is the Wigner–Seitz cell in FCC lattice, and it connects with all atoms in the nearest neighbour, which is the unit cell in the dual-lattice space as shown in Figure 8(b).

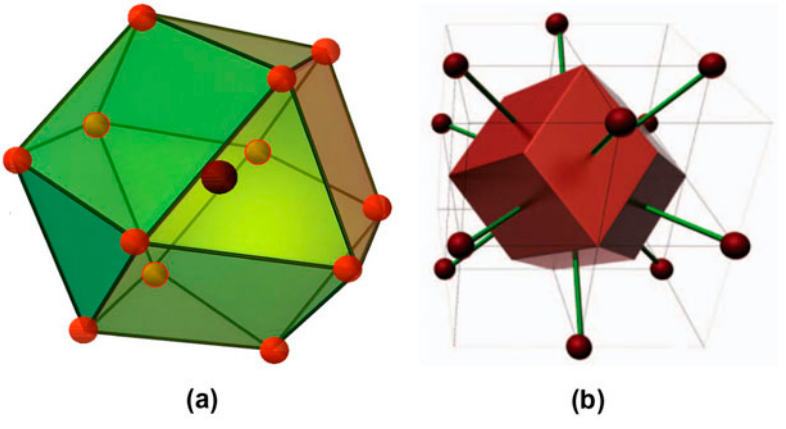

Figure 8. (colour online) (a) FCC unit cell (nearest neighbour), and (b) FCC Wigner–Seitz cell.

From Figure 8(a), one may find that a FCC dual-lattice tessellation unit is connected to 13 rhombic dodecahedron-shaped process zone elements, but only one of them belongs entirely to the unit. The rest 12 of the rhombic dodecahedron-shaped process zone elements belong to the 12 adjacent tessellation units. Recall that the rhombic dodecahedron is a scaled Wigner-Seitz cell, which we label as the 3^{rd} order process zone.

To build a MCDD DLPZ tessellation, we scale down the rhombic dodecahedron process zone from its original size. We then need twelve prism process zone elements to connect the 12 neighbouring 3^{rd} order process zone elements. They correspond to 12 congruent rhombic facets of the rhombic dodecahedron. We label these 12 prism-shaped process zone elements as the second-order process zone. There are 24 planar stacking fault process zone elements that connect to 24 edges in the rhombic dodecahedron element. We label 24 stacking fault process zone elements as the first-order process zone element. The physical meaning of the 24 stacking fault process zone elements are the 24 extended slip surfaces of eight independent slip systems in {1 1 1} family. To fill the rest of the space in the interior of the FCC tile unit cornered by the 13 rhombic dodecahedron process zone elements, we need 14 tetrahedron bulk crystal elements, and each of them connects to one vertex of the 14 vertices of the rhombic dodecahedron element. We call these 14 tetrahedron bulk crystal element as the 0th-order process zone element, or the bulk crystal element. The structure of FCC dual-lattice element unit is a homotopy of a conventional FCC crystal unit cell, and it is a scaled version of FCC crystal unit cell built with a hierarchy of different process zones. Figure 9 displays all types of process zone elements as well as bulk crystal elements in an FCC unit cell.

In passing, we note that Figure 9(i) shows a typical Thompson Tetrahedron structure presented in FCC lattice. To exam the detailed connections among different order process zone elements, we display the process zone connections with the centre rhombic dodecahedron process zone element in Figure 10.

Last, we note that the algebraic structure of FCC DLPZ involves: 14 bulk crystal elements, 24 stacking fault process zone elements and 12 prism shape process zone elements, and they connect to the 14 vertices, 24 edges and 12 facets of the centre rhombic dodecahedron element, which again confirms the well-known Euler's polyhedron formula in algebraic topology,

$$V - E + F = 2, \quad \text{in FCC DLPZ} :\Rightarrow \quad 14 - 24 + 12 = 2\,!$$

This indicates a perfect formation of a FCC crystal super dual-lattice tessellation. Moreover, FCC dual-lattice tessellation is irregular. For the 14 vertices of the center rhombic dodecahedron element, 6 of them are adjacent to 3 rhombic prism elements, 3 thin layer elements, and 1 tetrahedron element; whereas 8 of them are adjacent to 4 rhombic prism elements, 4 thin layer elements, and 1 tetrahedron element. When all elements are glued together, a global view of a complete FCC dual-lattice tessellation is shown in Figure 11.

Finally, we would like to point out that the dual-lattice process zone solid is not a crystal lattice structure, because the nodes of the process zone tessellation only form a quasi-crystal lattice [53]. The essence of this work is to use quasi-lattice structure to represent the crystal lattice and the possible defect presence in the lattice, whose motion is what we intend to study. By doing so, the dual-lattice process zone solid provides a multiscale material model that helps us study defect motions or evolutions inside the physical lattice space.

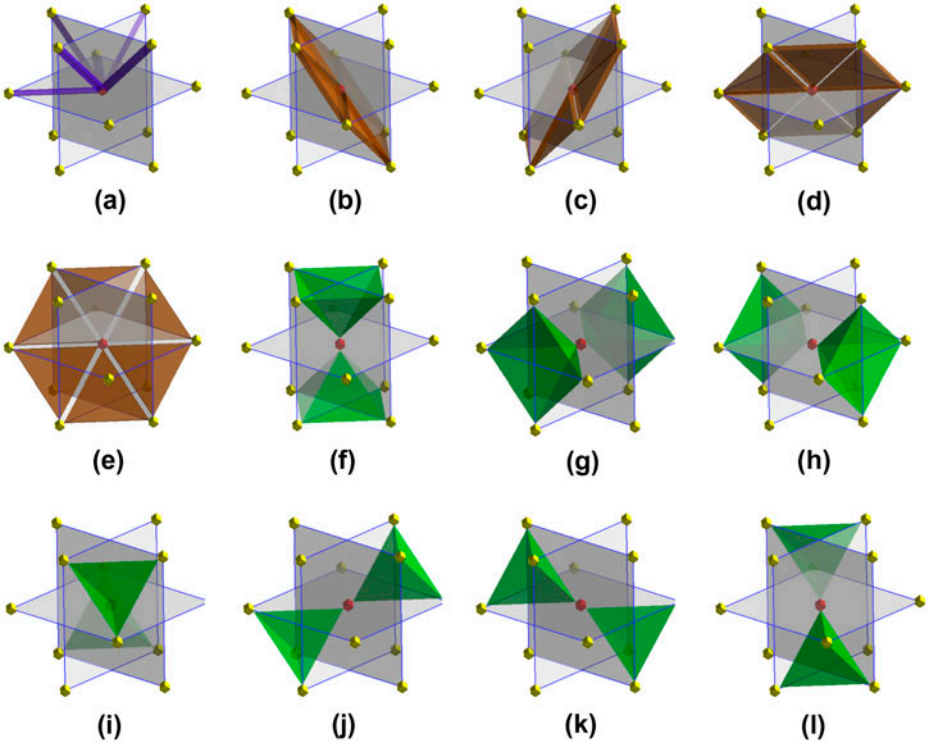

Figure 9. (colour online) (a) There are 13 third-order process zone elements and 12 second-order process zone elements (only six of them are shown); (b)–(e) 24 first-order stacking fault process zone elements; and (f)–(l) 14 bulk crystal elements (0th-order process zone) in a minimum FCC super dual-lattice tessellation unit.

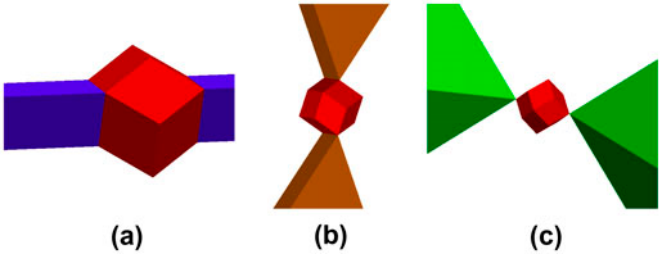

Figure 10. (colour online) Detailed connections between different order process zones in FCC crystals.

4. Higher order Cauchy–Born rule and multiscale modelling

To this end, we have developed a technical procedure to systematically establish a hierarchical order of process zone elements for both BCC and FCC crystals. In this section, we shall focus on the task: *How to model the constitutive relations inside the process zones*. In MCDD, we model the constitutive behaviours of the dual-lattice process zone by using an

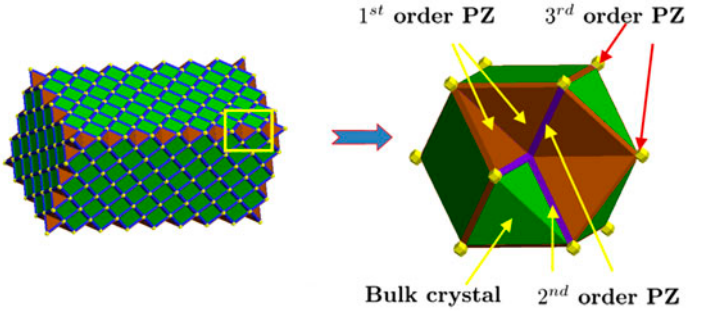

Figure 11. (colour online) A FCC dual-lattice tile: (a) FCC process zone tile, and (b) A FCC super dual-lattice tile unit.

atomistic-informed strain gradient theory. For general information regarding the atomistic-informed strain gradient theory, the readers may consult papers of [54,55,61]. However, in this work, we shall employ a fourth-order atomistic-informed strain gradient theory, which is far beyond the scope of the above-mentioned works.

4.1. *Hierarchical high-order Cauchy–Born rule*

Based on the kinematic assumption of MCDD, the tetrahedron bulk element is only subjected to uniform deformation, and all the non-linear deformations are confined in various process zone elements. We then set up the following atomistic-informed multiscale constitutive relations in each element type via a hierarchical higher order Cauchy–Born rule: **(1)** In the bulk tetrahedron elements, the deformation is assumed to be uniform, and the deformation gradient in each bulk crystal element, $\mathbf{F}_e = \dfrac{\partial \mathbf{x}}{\partial \mathbf{X}}\Big|_{\mathbf{X}\in\Omega_e^b}, e = 1, \cdots, n_{elem}^b$, will be a constant tensor. Hence, an arbitrary deformed bond vector $\mathbf{r}$ in a crystal unit cell of a given bulk element can be found by mapping the undeformed bond vector $\mathbf{R}$ to the deformed vector,

$$\mathbf{r} = \mathbf{F}\mathbf{R}. \tag{1}$$

we can then calculate the elastic strain energy density in a bulk element by calculating the strain energy density of an arbitrary unit cell inside the element,

$$W = \frac{1}{\Omega_0^u}\sum_{i=1}^{n_b}\phi(r_i) = \frac{1}{\Omega_0^u}\sum_{i=1}^{n_b}\phi(\mathbf{F}\mathbf{R}_i) = W(\mathbf{F}) \tag{2}$$

where $r_i = |\mathbf{r}_i|$. Note that the superscript u refers that Ω_0^u is the volume of the unit cell in the referential configuration, $\phi(r_i)$ is the atomistic potential and $r_i, i = 1, 2, \cdots, n_b$ are the current bond lengths in a unit cell, where the bond vector $\mathbf{r}_i$ is the distance vector between the centre atom in the unit cell and one of the atoms located at a vertex of the unit cell. Note that when calculating strain energy, the unit cell refers to the unit cell at atomistic scale, which is not the tile unit nor super dual-lattice Wigner–Seitz cell. In MCDD computations, a super dual-lattice Wigner–Seitz cell can be very large, and it may contain thousands of atoms. **(2)** In the first-order process zone, i.e. thin plate interphase process zone element,

we employ the second-order Cauchy–Born rule to extrapolate the strain gradient-based constitutive relation,

$$\mathbf{r} = \mathbf{F}\cdot\mathbf{R} + \frac{1}{2}\mathbf{G} : (\mathbf{R}\otimes\mathbf{R}), \quad \text{with } \mathbf{G} = \frac{\partial^2\mathbf{x}}{\partial\mathbf{X}\otimes\partial\mathbf{X}} = \frac{\partial\mathbf{F}}{\partial\mathbf{X}}$$

Taking into account the strain gradient effect on strain energy, we find that

$$W = \frac{1}{\Omega_0^u}\sum_{i=1}^{n_b}\phi(r_i) = \frac{1}{\Omega_0^u}\sum_{i=1}^{n_b}\phi\left(\left|\mathbf{F}\cdot\mathbf{R}_i + \frac{1}{2}\mathbf{G} : (\mathbf{R}_i\otimes\mathbf{R}_i)\right|\right) = W(\mathbf{F},\mathbf{G}) \tag{3}$$

(3) For the second-order process zone elements, i.e. the prism-like elements, we employ the third-order Cauchy–Born rule to establish the constitutive relation inside the process zone,

$$\mathbf{r} = \mathbf{F}\cdot\mathbf{R} + \frac{1}{2!}\mathbf{G} : (\mathbf{R}\otimes\mathbf{R}) + \frac{1}{3!}\mathbf{H}\vdots(\mathbf{R}\otimes\mathbf{R}\otimes\mathbf{R})$$

with

$$\mathbf{H} = \frac{\partial^3\mathbf{x}}{\partial\mathbf{X}\otimes\partial\mathbf{X}\otimes\partial\mathbf{X}} = \frac{\partial^2\mathbf{F}}{\partial\mathbf{X}\otimes\partial\mathbf{X}} = \frac{\partial\mathbf{G}}{\partial\mathbf{X}}$$

The free-energy density inside the second-order process zone elements are postulated as $W = W(\mathbf{F},\mathbf{G},\mathbf{H})$. **(4)** For the third-order process zone elements, or the polyhedra process zone elements, we adopt the fourth-order Cauchy–Born rule to model its constitutive behaviours,

$$\mathbf{r} = \mathbf{F}\cdot\mathbf{R} + \frac{1}{2!}\mathbf{G} : (\mathbf{R}\otimes\mathbf{R}) + \frac{1}{3!}\mathbf{H}\vdots(\mathbf{R}\otimes\mathbf{R}\otimes\mathbf{R}) + \frac{1}{4!}\mathbf{K} :: (\mathbf{R}\otimes\mathbf{R}\otimes\mathbf{R}\otimes\mathbf{R})$$

with

$$\mathbf{K} = \frac{\partial^4\mathbf{x}}{\partial\mathbf{X}\otimes\partial\mathbf{X}\otimes\partial\mathbf{X}\otimes\partial\mathbf{X}} = \frac{\partial^3\mathbf{F}}{\partial\mathbf{X}\otimes\partial\mathbf{X}\otimes\partial\mathbf{X}} = \frac{\partial^2\mathbf{G}}{\partial\mathbf{X}\otimes\partial\mathbf{X}} = \frac{\partial\mathbf{H}}{\partial\mathbf{X}}$$

and the free-energy density in the third-order process zone element is postulated to have the following form,

$$W = W(\mathbf{F},\mathbf{G},\mathbf{H},\mathbf{K}).$$

For metallic FCC crystals, one may use the embedded atom method (EAM) to calculate the interatomic force. The potential energy density inside a unit cell (not the Wigner–Seitz cell) can be written as,

$$W = \frac{1}{\Omega_0^u}\left(\sum_i F(\bar{\rho}_i) + \frac{1}{2}\sum_i\sum_{j\neq i}\phi(r_{ij})\right), \quad r_{ij} = |\mathbf{r}_j - \mathbf{r}_i|, \tag{4}$$

where the superscript u in Ω indicates that Ω_0^u is a unit cell. The host electron density at the atom site $\mathbf{x}_i$ is a function of the electron density,

$$\bar{\rho}_i = \sum_{j\neq i}\rho(r_{ij}).$$

For the Bravais lattice, there is only one atom in the centre of the unit cell, the potential energy density inside the unit cell may be simplified as,

$$W = \frac{1}{\Omega_0^u}\left(F(\bar{\rho}) + \frac{1}{2}\sum_j\phi(r_j)\right), \quad \bar{\rho} = \sum_j\rho(r_j).$$

where the integer j is the index of pair potential bond number in a unit call. Consequently, constitutive relations in all types of DLPZ elements can be established. For example, in the bulk crystal element (0th-order process zone element), the first Piola–Kirchhoff stress tensor can be obtained as following,

$$\mathbf{P} = \frac{\partial W}{\partial \mathbf{F}} = \frac{1}{\Omega_0^u} \sum_{j=1}^{n_b} \Big(F'(\bar{\rho}) \rho'(r_j) + \frac{1}{2} \phi'(r_j) \Big) \frac{\mathbf{r}_j \otimes \mathbf{R}_j}{r_j}, \tag{5}$$

where n_b is the total number of the bonds in the unit cell. Similarly, we can find the second Piola–Kirchhoff stress tensor and the Cauchy stress tensor in the bulk element as well,

$$\mathbf{S} = \frac{1}{\Omega_0^u} \sum_{j=1}^{n_b} \Big(F'(\bar{\rho}) \rho'(r_j) + \frac{1}{2} \phi'(r_j) \Big) \frac{\mathbf{R}_j \otimes \mathbf{R}_j}{r_j} \tag{6}$$

$$\boldsymbol{\sigma} = \frac{1}{\Omega_0^u} \sum_{j=1}^{n_b} \Big(F'(\bar{\rho}) \rho'(r_j) + \frac{1}{2} \phi'(r_j) \Big) \frac{\mathbf{r}_j \otimes \mathbf{r}_j}{r_j}. \tag{7}$$

The fourth-order elastic tensor can be also obtained as,

$$\mathbf{C} = \frac{\partial^2 W}{\partial \mathbf{E} \otimes \partial \mathbf{E}} \Big|_{\mathbf{E}=0} = \frac{1}{\Omega_0} \left\{ \sum_j \left[\frac{1}{2} \Big(\phi'' - \frac{1}{r_j} \phi' \Big) + F'(\bar{\rho}) \Big(\frac{\partial^2 \rho}{\partial r^2} - \frac{1}{r_j} \frac{\partial \rho}{\partial r} \Big) \right] \right.$$
$$\left. \times \frac{\mathbf{R}_j \otimes \mathbf{R}_j \otimes \mathbf{R}_j \otimes \mathbf{R}_j}{r_j^2} + F''(\bar{\rho}) \left(\sum_j \frac{\partial \rho}{\partial r} \frac{\mathbf{R}_j \otimes \mathbf{R}_j}{r_j} \right) \left(\sum_j \frac{\partial \rho}{\partial r} \frac{\mathbf{R}_j \otimes \mathbf{R}_j}{r_j} \right) \right\} \tag{8}$$

where $\mathbf{E} = (1/2)(\mathbf{F}^T \cdot \mathbf{F} - \mathbf{I})$ is the Green-Lagrangian strain, and $\mathbf{I}$ is the second-order unit tensor.

Inside the process zone, we must evaluate higher order stress couples,

$$\mathbf{Q} := \frac{\partial W}{\partial \mathbf{G}} = \frac{1}{2! \Omega_0^u} \sum_{j=1}^{n_b} \left(F'(\bar{\rho}_i) \rho'(r_j) + \frac{1}{2} \phi'(r_j) \right) \frac{\mathbf{r}_j \otimes \mathbf{R}_j \otimes \mathbf{R}_j}{r_j} \tag{9}$$

$$\mathbf{U} := \frac{\partial W}{\partial \mathbf{H}} = \frac{1}{3! \Omega_0^u} \sum_{j=1}^{n_b} \left(F'(\bar{\rho}_i) \rho'(r_j) + \frac{1}{2} \phi'(r_j) \right) \frac{\mathbf{r}_j \otimes \mathbf{R}_j \otimes \mathbf{R}_j \otimes \mathbf{R}_j}{r_j} \tag{10}$$

$$\mathbf{V} := \frac{\partial W}{\partial \mathbf{K}} = \frac{1}{4! \Omega_0^u} \sum_{j=1}^{n_b} \left(F'(\bar{\rho}) \rho'(r_j) + \frac{1}{2} \phi'(r_j) \right) \frac{\mathbf{r}_j \otimes \mathbf{R}_j \otimes \mathbf{R}_j \otimes \mathbf{R}_j \otimes \mathbf{R}_j}{r_j}, \tag{11}$$

according to the order of a given process zone.

5. MCDD finite element formulation

Let $\dot{\mathbf{u}}(\mathbf{X})$ be the velocity field in the continuum. We define the kinetic energy of the crystalline solid as,

$$\mathcal{T} = \int_V \frac{1}{2} \rho \dot{\mathbf{u}} \cdot \dot{\mathbf{u}} dV$$

where ρ is the mass density. We also denote the internal free energy of crystal continuum as

$$\mathcal{W}_{int} := \int_V W(\mathbf{F}, \mathbf{G}, \mathbf{H}, \mathbf{K}) dV.$$

where $W(\cdot)$ is the strain and strain gradient energy density. The Hamilton principle may then be written in terms of displacement variation for the fixed time interval between t_0 and t_1,

$$\delta \int_{t_0}^{t_1} (\mathcal{T} - \mathcal{W}_{int}) dt + \int_{t_0}^{t_1} \delta \mathcal{W}_{ext} dt = 0 \tag{12}$$

where $\mathcal{W}_{ext}$ is the external potential energy. The variation of kinetic energy is,

$$\delta \mathcal{T} = \int_V \rho \dot{\mathbf{u}} \cdot \delta \dot{\mathbf{u}} dV,$$

and the internal virtual work is,

$$\delta \mathcal{W}_{int} = \int_V \left\{ \frac{\partial W}{\partial \mathbf{F}} : \delta \mathbf{F} + \frac{\partial W}{\partial \mathbf{G}} \vdots \delta \mathbf{G} + \frac{\partial W}{\partial \mathbf{H}} :: \delta \mathbf{H} + \frac{\partial W}{\partial \mathbf{K}} \vdots\vdots \delta \mathbf{K} \right\} dV \tag{13}$$

Successive integration by parts yields the following expression,

$$\begin{aligned}
\delta \mathcal{W}_{int} = & - \int_V \nabla_X \cdot \left\{ \mathbf{P} - \nabla_X \cdot \left[\mathbf{Q} - \nabla_X \cdot \left(\mathbf{U} - \nabla_X \mathbf{V} \right) \right] \right\} \cdot \delta \mathbf{u} dV \\
& + \int_{\partial V} \left\{ \mathbf{N} \cdot \left[\mathbf{P} - \nabla_X \cdot \left(\mathbf{Q} - \nabla_X \cdot (\mathbf{U} - \nabla_X \cdot \mathbf{V}) \right) \right] \right\} \cdot \delta \mathbf{u} dS \\
& + \int_{\partial V} \left\{ \mathbf{N} \cdot \left(\mathbf{Q} - \nabla_X \cdot (\mathbf{U} - \nabla_X \cdot \mathbf{V}) \right) \right\} : \delta \mathbf{F} dS \\
& + \int_{\partial V} \left(\mathbf{N} \cdot (\mathbf{U} - \nabla_X \cdot \mathbf{V}) \right) \vdots \delta \mathbf{G} dS \\
& + \int_{\partial V} \left((\mathbf{N} \cdot \mathbf{V} \right) :: \delta \mathbf{H} dS.
\end{aligned} \tag{14}$$

Without lose of generality, for simplicity, we assume that on the boundary of the crystalline solid the strain gradient effects may be negligible, so that we may simplify the high-order boundary conditions as:

$$\bar{\mathbf{P}} = \nabla_X \cdot \left(\mathbf{Q} - \nabla_X \cdot (\mathbf{U} - \nabla_X \cdot \mathbf{V}) \right), \quad \forall \mathbf{X} \in \partial V_t \tag{15}$$

$$\bar{\mathbf{Q}} = \nabla_X \cdot (\mathbf{U} - \nabla_X \cdot \mathbf{V}), \quad \forall \mathbf{X} \in \partial V_t \tag{16}$$

$$\bar{\mathbf{U}} = \nabla_X \cdot \mathbf{V}, \quad \forall \mathbf{X} \in \partial V_t \tag{17}$$

$$\bar{\mathbf{V}} = \mathbf{V}, \quad \forall \mathbf{X} \in \partial V_t \tag{18}$$

and $\bar{\mathbf{T}} := \mathbf{N} \cdot \bar{\mathbf{P}} \; \forall \mathbf{X} \in \partial V_t$. We assume that

$$\bar{\mathbf{Q}} \approx 0, \; \bar{\mathbf{U}} \approx 0, \; \bar{\mathbf{V}} \approx 0, \quad a.e. \; \forall \mathbf{X} \in \partial V_u, \tag{19}$$

Note that $\partial V = \partial V_t \bigcup \partial V_u$ and $\delta \mathbf{u} = 0, \forall \mathbf{X} \in \partial V_u$.

By doing so, the last three terms of the internal work may be neglected. The external virtual work of the system may be expressed as follows,

$$\delta \mathcal{W}_{ext} = \int_V \mathbf{b} \cdot \delta \mathbf{u} dV + \int_{\partial V_t} \bar{\mathbf{T}} \cdot \delta \mathbf{u} dS$$

where $\mathbf{b}$ is the body force and $\bar{\mathbf{T}}$ is the traction vector on ∂V_t. The dynamics equations of the continuous lattice system can be then written as,

$$\nabla_X \cdot \Big(\mathbf{P} - \nabla_X \cdot [\mathbf{Q} - \nabla_X \cdot (\mathbf{U} - \nabla_X \cdot \mathbf{V})]\Big) + \mathbf{b} = \rho \ddot{\mathbf{u}}, \quad \forall \mathbf{X} \in V, \tag{20}$$

with the boundary conditions: (15)–(18) and (19).

Based on the strong form of the crystal defect dynamics equations (Equation (20)), we can derive the Galerkin weak formulation of MCDD as follows,

$$\begin{aligned}
&\sum_{e=1}^{n_{elem}^{p_0}} \left\{ \int_{\Omega_{p_0}^e} \rho_0 \ddot{\mathbf{u}}^h \cdot \delta \mathbf{u} dV + \int_{\Omega_{p_0}^e} \mathbf{P} : \delta \mathbf{F}^h dV \right\} \\
&\quad + \sum_{e=1}^{n_{elem}^{p_1}} \left\{ \int_{\Omega_{p_1}^e} \rho_0 \ddot{\mathbf{u}}^h \cdot \delta \mathbf{u}^h dV + \int_{\Omega_{p_1}^e} \Big(\mathbf{P} : \delta \mathbf{F}^h dV + \mathbf{Q} \dot{:} \delta \mathbf{G}^h\Big) dV \right\} \\
&\quad + \sum_{e=1}^{n_{elem}^{p_2}} \left\{ \int_{\Omega_{p_2}^e} \rho_0 \ddot{\mathbf{u}}^h \cdot \delta \mathbf{u}^h dV + \int_{\Omega_{p_2}^e} \Big(\mathbf{P} : \delta \mathbf{F}^h + \mathbf{Q} \dot{:} \delta \mathbf{G}^h + \mathbf{U} :: \delta \mathbf{H}^h\Big) dV \right\} \\
&\quad + \sum_{e=1}^{n_{elem}^{p_3}} \left\{ \int_{\Omega_{p_3}^e} \rho_0 \ddot{\mathbf{u}}^h \cdot \delta \mathbf{u}^h dV + \int_{\Omega_{p_3}^e} \Big(\mathbf{P} : \delta \mathbf{F}^h + \mathbf{Q} \dot{:} \delta \mathbf{G}^h + \mathbf{U} :: \delta \mathbf{H}^h + \mathbf{V} \vdots \delta \mathbf{K}^h\Big) dV \right\} \\
&= \sum_{i=0}^{3} \sum_{e_i=1}^{n_{elem}^{p_i}} \left\{ \int_{\Omega_{p_i}^{e_i}} \rho_0 \mathbf{b} \cdot \delta \mathbf{u}^h dV \right\} + \sum_{e_0=1}^{n_{elem}^{p_0}} \int_{\partial_t \Omega_{p_0}^{e_0}} \bar{\mathbf{T}} \cdot \delta \mathbf{u}^h dS
\end{aligned} \tag{21}$$

where $\mathbf{b}$ is the body force, $\Omega_{p_i}^{e_i}$ is the e_i element in the pth process zone, $\partial_t \Omega_{p_i}^{e_i}$ is the interception between the traction boundary and the boundary of the e_ith element in the ith process zone Ω_{p_i}.

To avoid imposing higher order stress boundary condition, we may either let them vanish at the boundary or simply avoid the higher order process element overlap with traction boundary $\partial_t \Omega_0$.

Note that all kinematic fields with the superscript "h" are the fields derived from the FEA interpolation field rather than the exact value. The local FEA interpolation in an element of the ith-order process zone is expressed as,

$$\mathbf{u}^h(\mathbf{X}, t) = \sum_{I_i=1}^{n_{d_i}} N_{I_i}(\boldsymbol{\zeta}) \mathbf{d}_{I_i}(t), \quad i = 0, 1, 2, 3$$

where n_{d_i} is the number of total nodes in the element, and $i = 0, 1, 2, 3$ indicates the order of the process zone. Here we count the bulk crystal elements as the 0th-order process zone, the thin plate elements as the first-order process zone, the prism elements as the second-order process zone, and the Wigner–Seitz vertex element as the third-process zone.

The above FEM discretization is a generic form for any elements. In this way, we can use a unified weak formulation for all elements, and in numerical implementation we can set the higher order stress couples or strain gradients to zero inside the lower order process zone elements without changing the generic MCDD FEM formulation. Substituting FEM shape function in the Galerkin weak form, we can obtain the discrete dynamics FEA algebraic equations as follows,

$$\sum_{i=0}^{3}\sum_{e_i=1}^{n_{e_i}}\sum_{I_i=1}^{n_{d_i}}\int_{V_{e_i}}\left(\mathbf{P}\cdot\frac{\partial N_{I_i}}{\partial \mathbf{X}}+\mathbf{Q}:\frac{\partial^2 N_{I_i}}{\partial \mathbf{X}\otimes\partial \mathbf{X}}\right.$$
$$\left.+\mathbf{U}\vdots\frac{\partial^3 N_{I_i}}{\partial \mathbf{X}\otimes\mathbf{X}\otimes\partial \mathbf{X}}+\mathbf{V}::\frac{\partial^4 N_{I_i}}{\partial \mathbf{X}\otimes\mathbf{X}\otimes\partial \mathbf{X}\otimes\partial \mathbf{X}}\right)\cdot\delta\mathbf{d}_{I_i}dV$$
$$+\sum_{i=0}^{3}\sum_{e_i=1}^{n_{e_i}}\sum_{I_i=1}^{n_{d_i}}\int_{V_{e_i}}\mathbf{b}N_{I_i}(\mathbf{X})\cdot\delta\mathbf{d}_{I_i}dV$$
$$+\sum_{e_0=1}^{n_{e_0}}\sum_{I_0=1}^{n_{d_0}}\int_{\partial V_{e_0}}\bar{\mathbf{T}}N_{I_0}(\mathbf{X})\cdot\delta\mathbf{d}_{I_0}dS$$
$$+\sum_{i=0}^{3}\sum_{e_i=1}^{n_{e_i}}\sum_{I_i,J_i=1}^{n_{d_i}}\int_{V_{e_i}}\rho N_{I_i}(\mathbf{X})N_{J_i}(\mathbf{X})\ddot{\mathbf{d}}_{J_i}\cdot\delta\mathbf{d}_{I_i}dV=0. \tag{22}$$

In a representative element e, we define the following FEM *matrix tensors*,

$$\frac{\partial \mathbf{u}}{\partial \mathbf{X}}=\sum_{I=1}^{n_{d_i}}\frac{\partial N_{I_i}}{\partial \mathbf{X}}\mathbf{d}_{I_i}=:\mathbf{B}_{e_i}(\mathbf{X})\mathbf{d}_{e_i},\quad \mathbf{X}\in\Omega_{e_i} \tag{23}$$

$$\frac{\partial^2 \mathbf{u}}{\partial \mathbf{X}\otimes\partial \mathbf{X}}=\sum_{I_i=1}^{n_{d_i}}\frac{\partial^2 N_{I_i}}{\partial \mathbf{X}\otimes\partial \mathbf{X}}\mathbf{d}_{I_i}=:\mathbf{C}_e(\mathbf{X})\mathbf{d}_e,\quad \mathbf{X}\in\Omega_e \tag{24}$$

$$\frac{\partial^3 \mathbf{u}}{\partial \mathbf{X}\otimes\partial \mathbf{X}\otimes\partial \mathbf{X}}=\sum_{I_i=1}^{n_{d_i}}\frac{\partial^3 N_{I_i}}{\partial \mathbf{X}\otimes\partial \mathbf{X}\otimes\partial \mathbf{X}}\mathbf{d}_{I_i}=:\mathbf{D}_{e_i}(\mathbf{X})\mathbf{d}_{e_i},\quad \mathbf{X}\in\Omega_{e_i} \tag{25}$$

$$\frac{\partial^4 \mathbf{u}}{\partial \mathbf{X}\otimes\partial \mathbf{X}\otimes\partial \mathbf{X}\otimes\partial \mathbf{X}}=\sum_{I_i=1}^{n_{d_i}}\frac{\partial^4 N_{I_i}}{\partial \mathbf{X}\otimes\partial \mathbf{X}\otimes\partial \mathbf{X}\otimes\partial \mathbf{X}}\mathbf{d}_{I_i}=:\mathbf{E}_{e_i}(\mathbf{X})\mathbf{d}_{e_i},\ \mathbf{X}\in\Omega_{e_i} \tag{26}$$

where $e_i=1,\cdots,n_{e_i}$ and,

$$\mathbf{d}_e(t)=\left[\mathbf{d}_1(t),\cdots,\mathbf{d}_{n_{d_i}}(t)\right]^T$$

is the element nodal displacement vector, and $\mathbf{B}_{e_i}$, $\mathbf{C}_{e_i}$, $\mathbf{D}_{e_i}$ and $\mathbf{E}_{e_i}$ are element interpolation gradient, the second gradient, the third gradient and the fourth gradient *matrix tensors*! When we say that $\mathbf{B}_{e_i}$ is a first-order tensor matrix, i.e. $\mathbf{B}_{e_i}$ is a vector matrix or a matrix with its each entry as the first-order tensor; similarly $\mathbf{C}_{e_i}$ is a second-order tensor matrix, $\mathbf{D}_{e_i}$ is a third-order tensor matrix, and $\mathbf{E}_{e_i}$ is a fourth-order tensor matrix. Following the standard FE discretization procedure, e.g. [29], we can obtain the following discrete crystal defect dynamic equations of motion of crystal bundles,

$$\mathbf{M}\ddot{\mathbf{d}}+\mathbf{f}^{int}(\mathbf{d})=\mathbf{f}^{ext} \tag{27}$$

where

$$\mathbf{M} = \sum_{i=0}^{3} \overset{n_{e_i}}{\underset{e_i=1}{\boldsymbol{A}}} \int_{V_0^{e_i}} \rho_0 \mathbf{N}_{e_i}{}^T \mathbf{N}_{e_i} dV \tag{28}$$

$$\mathbf{f}^{int} = \sum_{i=0}^{3} \overset{n_{e_i}}{\underset{e_i=1}{\boldsymbol{A}}} \int_{V_0^{e_i}} \left(\mathbf{V}_{e_i}{}^T \cdot \mathbf{P}_{e_i} + \mathbf{C}_{e_i}^T \cdot \mathbf{Q}_{e_i} + \mathbf{D}_{e_i}^T \cdot \mathbf{U}_{e_i} + \mathbf{E}_{e_i}^T \cdot \mathbf{V}_{e_i} \right) dV \tag{29}$$

$$\mathbf{f}^{ext} = \sum_{i=0}^{3} \overset{n_{e_i}}{\underset{e_i=1}{\boldsymbol{A}}} \left\{ \int_{V_{p_i}^{e_i}} \mathbf{N}_{e_i}{}^T \rho_0 \mathbf{b} dV + \int_{\partial_t V_{p_i}^{e_i}} \mathbf{N}_{e_i}{}^T \bar{\mathbf{T}}^{e_i} dS \right\} \tag{30}$$

where $\overset{n_{e_i}}{\underset{e_i=1}{\boldsymbol{A}}}$ is the element assemble operator [29], and

$$\mathbf{N}_{e_i} = \left[N_1(\mathbf{X}), \cdots, \mathbf{N}_{n_{e_i}}(\mathbf{X}) \right]^T$$

is the element shape function matrix. Note that in lower order process zones, the elemental shape function matrices, $\mathbf{C}_{e_i}$, $\mathbf{D}_{e_i}$ and $\mathbf{E}_{e_i}$ are set to zero.

The explicit Newmark-β time integration algorithm ($\beta = 0$) [5] is used in the kinematics update,

$$\mathbf{d}_{n+1} = \mathbf{d}_n + \mathbf{v}_n \Delta t + \frac{1}{2} \mathbf{a}_n \Delta t^2 \tag{31}$$

$$\mathbf{a}_{n+1} = \mathbf{M}^{-1} \left(\mathbf{f}_{n+1}^{ext} - \mathbf{f}_{n+1}^{int} \right) \tag{32}$$

$$\mathbf{v}_{n+1} = \mathbf{v}_n + \frac{1}{2} (\mathbf{a}_n + \mathbf{a}_{n+1}) \Delta t \tag{33}$$

where $\mathbf{d}_n$ is the displacement field at the time step n, $\mathbf{v}_n$ is the velocity field at the time step n, and $\mathbf{a}_n$ is the acceleration field at the time step n and Δt is time increment. The subscript n and $n+1$ denote to quantities evaluated at time t_n and t_{n+1}. In MCDD, the bulk crystal element and the process zone elements form a scale-up super lattice structure that resembles the original fine scale dual-lattice structure. In our construction, the order of the process zone element corresponds to the order of strain gradients that are used in the constitutive modelling of the process zone.

In MCDD, different order process zone elements of same crystal is assigned to the same atomistic potential in the construction of constitutive relations, but the kinematic and constitutive constrains vary in different order of process zones. That is: the bulk crystal element only has uniform deformation, which is modelled by the first-order Cauchy–Born rule; whereas non-linear deformation is confined in the process zone elements, which are modelled by various higher order strain gradient Cauchy–Born rules. This will define specific length scale in the specific process zone according to the specific order of the strain gradients, which is the primary reason why we coin the method as the *Multiscale* Crystal Defect Dynamics, because in three-dimensional crystal lattices we shall have at least three different length scales corresponding to three different order of process zones. Based on the construction, the process zone element family has three different length scales corresponding to three different order of process zones: The interphase element can accommodate linear strains, the prism process zone element allows the second-order strain distribution, and the void type process zone element has non-zero third-order strain gradient distributions.

Consequently, the mesoscale constitutive relation for process zone elements at different scales will behave differently. In this work, we postulate a fundamental hypothesis of multiscale crystal defect mechanics: *For a perfect crystal under external loads, the material will always fail first at where the deformation state becomes inhomogeneous.*

To test the postulate, we perform a benchmark test to validate the hypothesis. The benchmark test is performed on a quadrilateral element Figure 12(a). We use three different order Cauchy–Born rule-based constitutive relations in quadrilateral element, i.e. the first-order Cauchy–Born rule-based constitutive relation, the second-order Cauchy–Born rule-based constitutive relation and the third-order Cauchy–Born rule-based constitutive relation. Since the bilinear quadrilateral element (Q4) can only reproduce bilinear polynomials, and it cannot support strain gradients, for the second-order Cauchy–Born rule-based and the third-order Cauchy–Born rule-based constitutive relations, we add a bubble function mode, $N_5(\xi, \eta)$, inside the Q4 element, i.e.

$$
\begin{aligned}
N_1(\xi,\eta) &= \frac{1}{4}(1-\xi)(1-\eta) - \frac{1}{4}N_5(\xi,\eta)\\
N_2(\xi,\eta) &= \frac{1}{4}(1+\xi)(1-\eta) - \frac{1}{4}N_5(\xi,\eta)\\
N_3(\xi,\eta) &= \frac{1}{4}(1+\xi)(1+\eta) - \frac{1}{4}N_5(\xi,\eta)\\
N_4(\xi,\eta) &= \frac{1}{4}(1-\xi)(1+\eta) - \frac{1}{4}N_5(\xi,\eta)\\
N_5(\xi,\eta) &= (1-\xi^2)(1-\eta^2)
\end{aligned}
$$

In Figure 12, one may find that in a same element the peak force value for the third-order Cauchy–Born rule-based stress–strain law is the lowest, and the peak force value for the second-order Cauchy–Born rule-based stress-strain law is the second lowest and the peak force value for the first Cauchy–Born rule is the highest. This test has clearly demonstrated that the higher order non-linearity of the constitutive model, the lower strength of the constitutive model. This implies that the process zone element will always fail first, and the higher order strain gradient a process zone has, the lower strength it has. In most

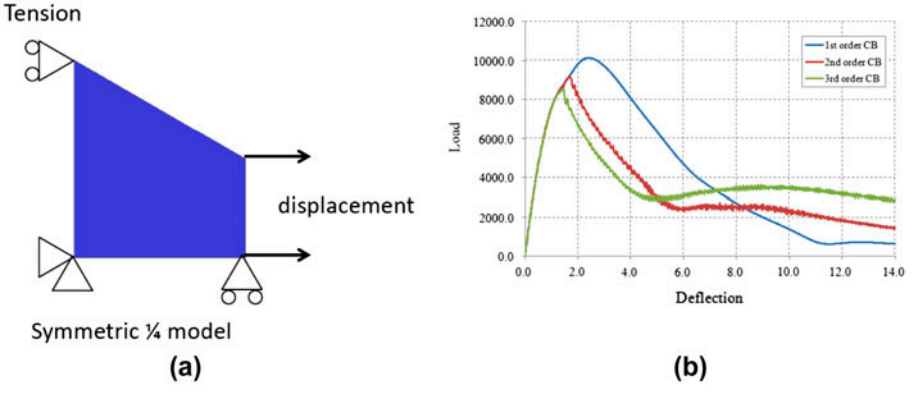

Figure 12. (colour online) Constitutive behaviours of different order of process zone elements: (a) Benchmark test, and (b) Test results.

MCDD FEM mesh constructions, we choose a subset of atoms as the representative atoms to make a super lattice, which only contains part of lattice slip planes in the crystal space; and then build the corresponding super dual lattice and finally expand it into the super DLPZ tiling, which includes stacking fault interphase elements, prism elements and vertex elements. By doing so, it allows simulations of real and finite size defects and their motions. More precisely speaking, the a priori chosen process zone tessellation is intrinsically built, and it is kinematically favourable for non-linear finite deformations, and therefore it will automatically allow defect nucleation, evolution, propagation and growth.

6. Simulation examples

To validate the proposed MCDD method, in this section we present two examples of MCDD simulations and the comparison between the results of MCDD simulations and that of molecular dynamics.

6.1. *Example I: validation of MCDD in simulation of nanoindentation*

In the first numerical example, we have employed MCDD to simulate a two-dimensional nanoindentation of single crystal of Cu, which had been carefully studied in the numerical simulations by using both molecular dynamics as well as interatomic potential finite element method (FEM) [67,68]. The FCC lattice microstructure in $(1\bar{1}0)$ plane has been briefly discussed by [50] before. Figure 13 shows a two-dimensional process zone FEM mesh (tiling) that can be created based on the two-dimensional FCC lattice structure on $(1\,\bar{1}\,0)$ plane, or one may create 2D DLPZ tiling by cutting a slice from a three-dimensional process zone FEM mesh (tiling) as shown in Figure 14. Following [68], we adopt a so-called EAM-Mishin potential for Copper (see: [44]), in which the pair potential in Equation (4) is given as,

$$\phi(r) = \Big(E_1 M(r, r_0^{(1)}, \alpha_1) + E_2 M(r, r_0^{(2)}, \alpha) + \delta\Big)\psi\Big(\frac{r - r_c}{h}\Big) - \sum_{n=1}^{3} H(r_s^{(n)} - r) S_n (r_s^{(n)} - r)^4$$

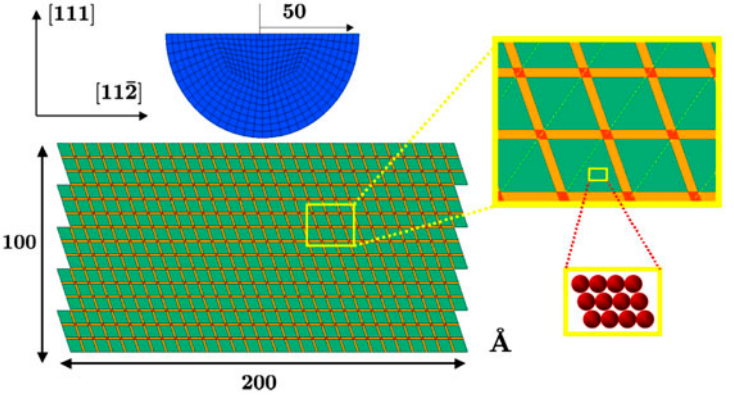

Figure 13. (colour online) Description of the nanoindentation problem.

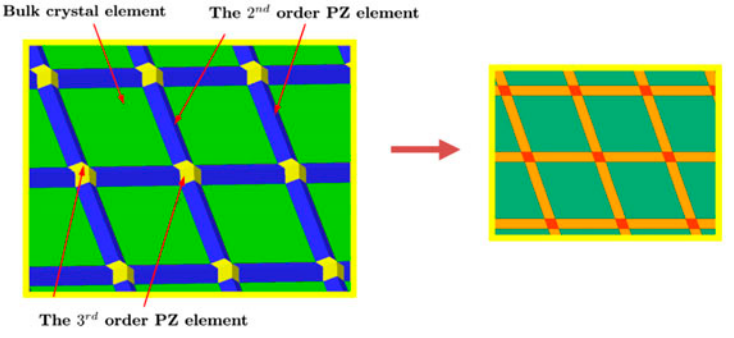

Figure 14. (colour online) Set-up of 2D process zone tiling (mesh) by projection of a 3D process zone FEM mesh onto $(1\,\bar{1}\,0)$ plane.

where

$$M(r, r_0, \alpha) = \exp[-2\alpha(r - r_0)] - 2\exp[-\alpha(r - r_0)]$$

is the Morse function, $H(\cdot)$ is the Heaviside function and is the cut-off function for the pair potential defined as,

$$\psi(x) = \begin{cases} 0, & x \geq 0 \\ \dfrac{x^4}{(1+x^4)}, & x < 0 \end{cases}.$$

The embedding function for the EAM-Mishin potential is given as,

$$F(\bar{\rho}) = \begin{cases} F^0 + \frac{1}{2}F^{(2)}(\bar{\rho}-1)^2 + \sum_{n=1}^{4} q_n(\bar{\rho}-1)^{n+2}, & \bar{\rho} < 1 \\ \dfrac{F^0 + \frac{1}{2}F^{(2)}(\bar{\rho}-1)^2 + q_1(\bar{\rho}-1)^3 + Q_1(\bar{\rho}-1)^4}{1 + Q_2(\bar{\rho}-1)^3}, & \bar{\rho} > 1 \end{cases} \tag{34}$$

which is the energy required to embed an atom into the electron density distribution. All the parameters in (34) are exactly the same as that in [44,68]. In particular, the host electron density in (34) at the atom site $\mathbf{r}_i$ is defined as,

$$\bar{\rho}_i = \sum_{j \neq i} \rho(r_{ij}), \quad r_{ij} = |\mathbf{r}_j - \mathbf{r}_i|,$$

where ρ is the electronic density function at each atom site, and it is given as

$$\rho(r) = \left[a \exp\left(-\beta_1 \left(r - r_0^{(3)}\right)^2\right) + \exp\left(-\beta_2 \left(r - r_0^{(4)}\right)\right)\right] \psi\left(\frac{r - r_c}{h}\right)$$

For the Bravais lattice, the host electron density at the centre of the unit cell is simply denoted as $\bar{\rho}$ (without i), and it may be calculated with respect to different groups of coordinate shells, i.e.

$$\bar{\rho} = \sum_{m} \sum_{j=1}^{N_m} \rho(r_j).$$

where m is the number of coordinate shells and N_m is the atom number in the mth shell. If we only consider the nearest neighbour interaction, $m = 1$. All the parameters used in the computation presented here are the same as that in [44,68] for single crystal copper. It may be noted that the function $\rho(r)$ is normalized so that in the equilibrium state $\bar{\rho} = 1$, i.e.

$$\bar{\rho}_0 = \sum_m N_m \rho_m(R_m) = 1. \tag{35}$$

where R_m and N_m are the radium and the number of atoms in the mth coordination shell. The pair potential ϕ should satisfy the mechanical equilibrium condition of the FCC crystal, i.e.

$$\sum_m N_m R_m \phi^{'}(R_m) = 0. \tag{36}$$

where Equations (35)–(36) determine equilibrium bond length and the parameter E_1. Before proceeding to the simulation, we first used the EAM-Mishin potential and the Cauchy–Born rule to calculate material parameters for the atomistic-enriched continuum model in order to validate the multiscale method. The calculated material constants for Cu are listed in Table 1 in comparison with the experimental data. The nanoindentation test is carried out on a 200 Å × 100 Å plane strain specimen, whose X-axis is along [1 1 $\bar{2}$] direction and whose Y-axis is along the [1 1 1] direction as shown in Figure 13. A rigid 2D cylindrical indenter whose axial direction is along the [1 $\bar{1}$ 0] direction (Z-axis) is imposed normal to the (1 1 1) plane. The radius R of the cylindrical rigid indenter is 50 Å, and the contact between the rigid indenter and Cu specimen is described by an external repulsive potential as discussed in [30,68]

$$\phi^{ext}(r) = AH(R - r)(R - r)^3$$

where A is a force constant and $H(r)$ is the step function. In the present calculations, $A = 10\,\text{eV/Å}$. The indentation proceeds in displacement control at a speed of about 1 m/s. The only difference in the contact algorithm between the present work and that of Zhu et al. [68] is that we have adopted a nanoscale coarse-grained adhesive contact algorithm developed by [51], whereas in [68] a prescribed analytical contact boundary condition is prescribed. One may note from the perspective of 3D projection (see Figure 14), the green bulk element, which can be a rhombic element or two triangle elements, is from the 3D bulk crystal element – a 0th-order process zone in 3D lattice; the orange element is from the second-order process zone in 3D lattice, and the small red rhombic element is from a third-order process zone in 3D lattice. However, in 2D MCDD simulations, some simplifications are being made; we still choose the 2D green bulk element as the 0th-order process zone, but we set the orange element as the first-order process zone, and we set the small red rhombic element as the second process zone. In the FEA model shown in Figure 13, there are 435 0-th order process zone elements (bulk crystal elements), 822 first-order process zone elements, and 288 second-order process zone elements. In Figure 15(a), we display the effective stress distribution on the single crystal (Cu) substrate, which has a pattern that is similar to that obtained via both the atomistic potential-based FEM as well as the molecular dynamics simulations Figure 15(b). In Figure 16, the load-deflection curve of nanoindentation is compared with that of both molecular dynamics and atomistic-potential finite element method (AP-FEM). There are several load-deflection curves obtained in MCDD simulation corresponding to different width of the first-order process zone. It has been shown that all the MCDD results obtained in the simulations

Table 1. Elastic constants for Cu.

	Experiment	(1st) neighbour	(2nd) neighbour	(3rd) neighbour	4th neighbour
C_{1111}	1.700	1.780	1.745	1.725	1.697
C_{1122}	1.225	1.101	1.256	1.251	1.223
C_{1212}	0.758	0.679	0.786	0.769	0.762

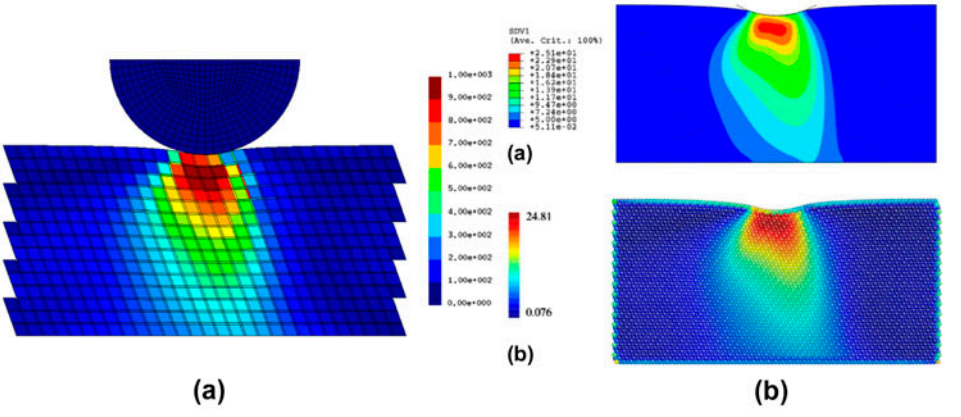

Figure 15. (colour online) The van Mises stress contour in the Cu substrate during indentation (a) MCDD result, and (b) Atomistic-potential FEA and MD results (Reuse permission by Elsevier: License Number 3057290919368).

can *automatically* predict dislocation nucleation induced elastic instability just as the MD simulation without calculations of eigenvalues of the acoustic tensor, whereas the atomistic-potential FEM is essentially incapable of such prediction because of its intrinsic kinematic restriction. This is because that first the AP-FEM meshes reported in [67,68] are incapable of capturing general crystal slips, and second the AP-FEM is ill-conditioned after it reaches to the critical bifurcation point, i.e. the system does not have any intrinsic length scales as the MCDD does, and hence it has no unique solution for dislocation burst and motion, and it allows multiple solutions or instability modes. To introduce material length scale, MCDD adopts a higher order strain gradient formulation, and it can be also accomplished by introducing various dissipation mechanisms such as heat conduction or diffusion. One of the challenges in nanoindentation simulations is to capture surface roughness of the substrate during the indentation, which is the manifestation of surface displacement burst caused by dislocation nucleation, and it is a distinct feature of nanoscale indentation. In Figure 17, we show the dislocation induced surface roughness captured by the MCDD simulation.

6.2. *Example II: simulation of fracture at atomistic scale*

In the second example, we apply MCDD to simulate fracture at atomistic scale, and compare the obtained results with that of molecular dynamics simulation [27]. This is a two-dimensional MCDD simulation within (1 1 1) plane of a FCC crystal (Copper) as

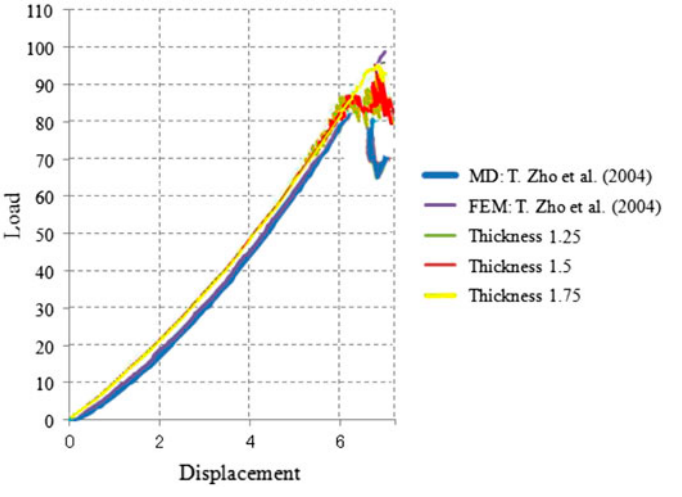

Figure 16. Load-deflection curve during indentation.

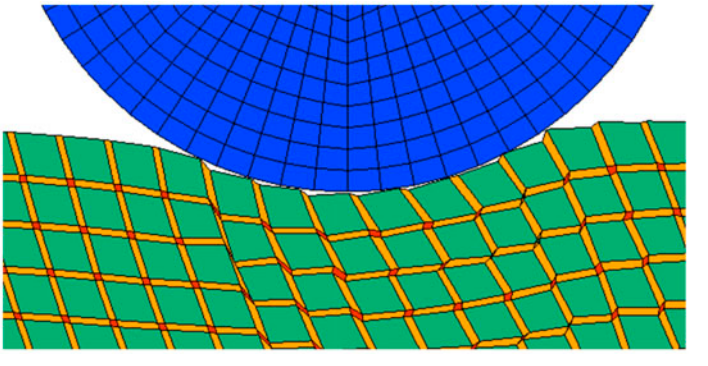

Figure 17. (colour online) Surface roughness captured in MCDD simulation.

shown in Figure 18. We prescribe a high strain rate boundary loading condition to initiate a mode-I fracture, which is based on the same boundary condition imposed in [27].

To do so, one may first create a three-dimensional FCC DLPZ tessellation, and one can then obtain the two-dimensional (1 1 1) plane process zone tiling by projecting the 3D DLPZ tessellation onto the (1 1 1) plane as shown in Figure 19. To coarsen the DLPZ tiling, we use a super DLPZ tiling with the same aspect ratio as that of the original DLPZ tiling, By doing so, we can create a three-level process zone tiling to cover the whole lattice plane without gap and overlap as shown in Figure 18(b).

The illustrated process zone construction process is revealing, because it shows that the 2D triangle bulk element is actually the projection of the first-order process zone element in a 3D super DLPZ tiling, instead of the projection of the 3D tetrahedron bulk crystal element; while the 2D rectangular element is the (1 1 1)-plane projection of the second-order process zone element (prism element) in 3D lattice, and the 2D honeycomb element is the projection of the 3D third-order process zone element (vertex element). This correspondence is indicated in Figure 19(b). Physically, this makes perfect sense because the (1 1 1) plane

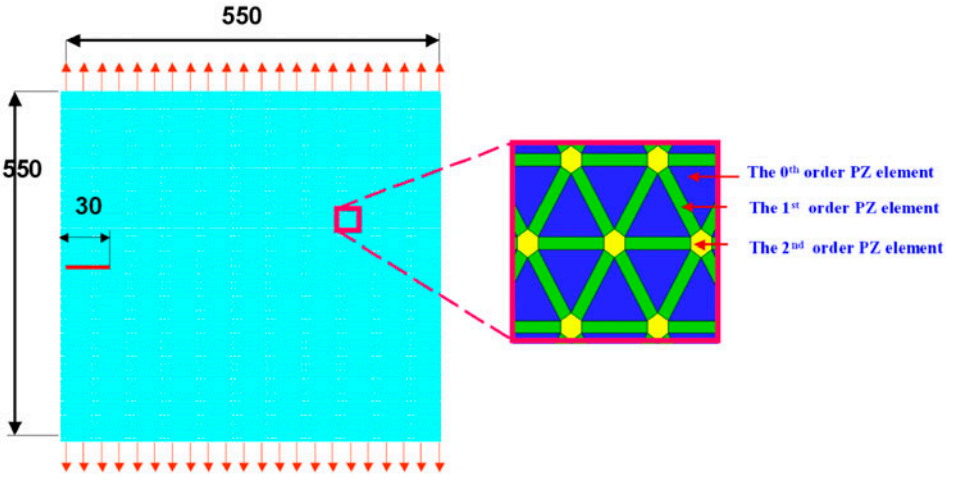

Figure 18. (colour online) Example II problem statement and MCDD process zone mesh.

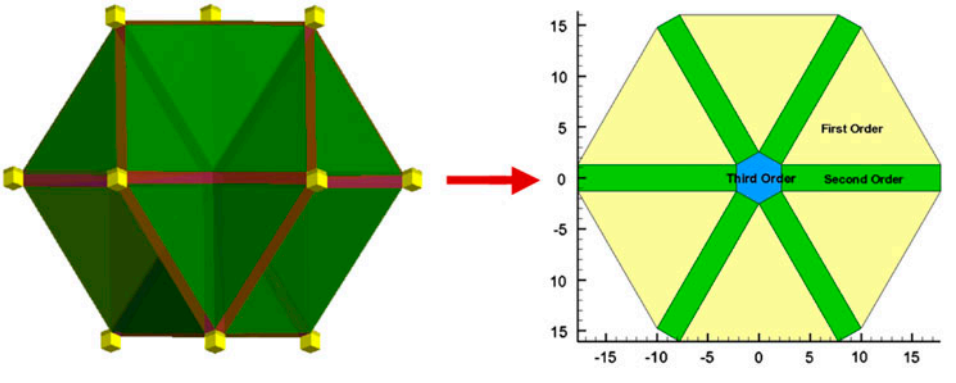

Figure 19. (colour online) FCC (1 1 1) plane projection of DLPZ tiling.

is the most susceptible slip plane in the FCC single crystal, so that the material on (1 1 1) plane must be weaker than that of bulk crystals. In this particular problem, we do not intend to exam the dislocation or crystal slip on (1 1 1) plane, but we would like to study ductile fracture within the (1 1 1) plane. Therefore, in this example, we assume that the triangle bulk element is governed by the first-order Cauchy–Born rule-based constitutive relation; the rectangular interphase element as the first process zone is governed by the second-order Cauchy–Born rule, and the honeycomb element as the first-order process zone is modeled by the third-order Cauchy–Born rule-based stress-strain relation. The simulation specimen of the two-dimensional MCDD computation is shown in Figure 18. Following [24], we have used an analytical EAM potential in the fracture simulation, which is exactly the same as that used in the molecular dynamics simulation [27],

$$W = \frac{1}{\Omega_0}\left((1-\chi F(\bar{\rho})) + \frac{1}{2}\chi \sum_j \phi(r_j)\right), \quad \text{where}$$

$$\phi(r) = r^{-12} - r^{-6}, \text{ and } F(\bar{\rho}) = \frac{E_{coh}}{\bar{\rho}_0}\bar{\rho}\ln\bar{\rho},$$

$$\bar{\rho} = \sum_j \rho(r_j), \quad \rho(r) = \begin{cases} \dfrac{\bar{\rho}_0}{d(d+1)}\left(\dfrac{r_m^2 - r^2}{r_m^2 - 1}\right)^2, & 0 < r < r_m \\ 0, & r \geq r_m \end{cases}$$

where $\bar{\rho}_0 = 1/e$, r_m is the cut-off radius, d is the space dimension, $0 \leq \chi \leq 1$ is the ratio of vacancy formation energy to cohesive energy; and the cohesive energy is given by $E_{coh} = \frac{1}{2}d(d+1)\epsilon$, and ϵ is the bond energy that is normalized as $\epsilon = mr_0^2/t_0^2$, in which m is the atomic mass, r_0 is the equilibrium bond length, and t_0 is the time unit. Note that in a preliminary study [38], we used the EAM-Mishin potential for Copper in the simulation instead of the above EAM potential. The finite element implementations of triangle elements and rectangular elements are straightforward implementation of linear triangle shape functions and bilinear quadrilateral shape functions. One may note that even though the bilinear quadrilateral element can only reproduce linear and the cross-term quadratic functions, for those interphase elements with non-zero rotation angles with respect to the global coordinate, one can still obtain non-zero strain gradients, which may trigger earlier material failure (than the bulk element) if the stress level is high enough. A non-trivial computation task is how to build FEA shape functions for the second-order process zone element, which is a hexagonal element. In this element, we employ the third-order Cauchy–Born rule to obtain its mesoscale constitutive relation, and we assume that the contribution of the second-order strain gradients to crystal defect motion is significant. Because this element may provide an defect model for microvoids and vacancies, we discuss it here in details. In the computation, we use a 6-node honeycomb Wachspress element [59] to model the hexagonal element, i.e. the second-order process zone element. We use the following local finite element interpolation field,

$$\mathbf{u}(X, Y, t) = \sum_{I=1}^{6} N_I(\xi, \eta)\mathbf{u}_I(t),$$

which is supported by the following Wachspress shape function,

$$N_i(\boldsymbol{\zeta}) = c_i \frac{\lambda_{i+2}(\boldsymbol{\zeta})\lambda_{i+3}(\boldsymbol{\zeta})\lambda_{i+4}(\boldsymbol{\zeta})\lambda_{i+5}(\boldsymbol{\zeta})}{q(\boldsymbol{\zeta})}, \quad i = 1, 2, 3, 4, 5, 6$$

where $\boldsymbol{\zeta} = (\xi, \eta)$, and

$$c_i = \frac{q(\boldsymbol{\zeta}_i)}{\lambda_{i+2}(\boldsymbol{\zeta}_i)\lambda_{i+3}(\boldsymbol{\zeta}_i)\lambda_{i+4}(\boldsymbol{\zeta}_i)\lambda_{i+5}(\boldsymbol{\zeta}_i)}$$

in which $\lambda_j(\boldsymbol{\zeta})$ is the expression of the linear algebraic equation representing the line segment connecting vertices $j-1$ and j. A circumference circle,

$$q(\boldsymbol{\zeta}) = \xi^2 + \eta^2 - R^2 = 0,$$

connects all the vertices as shown in Figure 20. Note that here $R = 2na$, a is the lattice bond length, and $n > 1$ is the scaling factor. For the parameters of the honeycomb element shown in Figure 20, we have the following exact values for c_i,

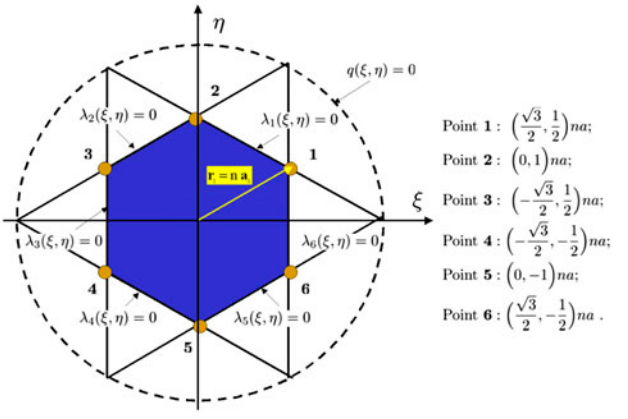

Figure 20. (colour online) The Washspress shape function for the honeycomb element.

$$c_1 = \frac{\sqrt{3}}{3}, c_2 = \frac{2}{3}, c_3 = -\frac{\sqrt{3}}{3}, c_4 = \frac{\sqrt{3}}{3}, c_5 = \frac{2}{3}, c_1 = -\frac{\sqrt{3}}{3} .$$

In this simulation, we have used a process zone tessellation model that consists of total 82,212 nodes, 27,404 bulk crystal elements (triangle element), 40,873 first-order process zone elements (interphase element), and 13,470 second-order process zone elements (hexagonal element) as shown in Figure 18. In comparison with a full molecular dynamics simulation of 300,000 atoms, the reduction in number of degrees of freedom in the MCDD simulation is about 1-to-4. Before the simulation, a pre-notched crack is created in the specimen, which has an initial length 30 in the reduced unit; the thickness of the interphase element is 0.32 in the reduced unit; the time increment of time integration is 0.0033 in the reduced unit, and the velocity imposed at top and bottom boundary is $0.03r_0/t$, which is corresponding to the strain rate of 1.12×10^{-4} in [27]. Figure 21 displays a time sequence of snapshots of crack propagation at different time instances obtained in a MCDD simulation, in which one may find that the crack bifurcates due to acoustic wave perturbation, which is reflected from the boundary. This is in a good agreement with the results obtained in MD simulation of exactly the same specimen, the same material, and the same loading conditions. In Figure 22, we compare the crack speed history (vs. time) obtained in a MCDD simulation with that obtained in a MD simulation [27]. One may see that except that MCDD predicts a slight early crack growth, it agrees with MD result well. In fact, the result presented here is better than our previous result obtained from an atomistic-informed interphase finite element calculation [24,38], in which we have conducted calculation for the same problem. In [24], only the first-order process zone is used, and the effect of the second-order process zone is neglected; and in [38] only the second derivatives of the shape function is considered, and the effect of the third-order derivatives of FEM shape is neglected, while calculating the strain gradient. The results obtained in both studies are far less accurate than that of the present study.

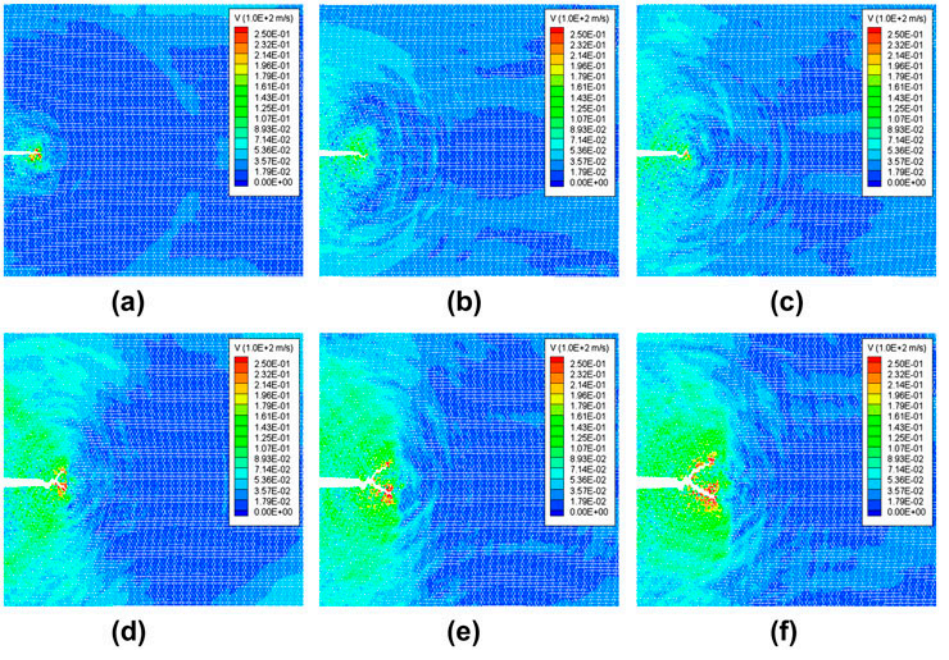

Figure 21. MCDD simulation result: Crack propagation sequence (velocity field).

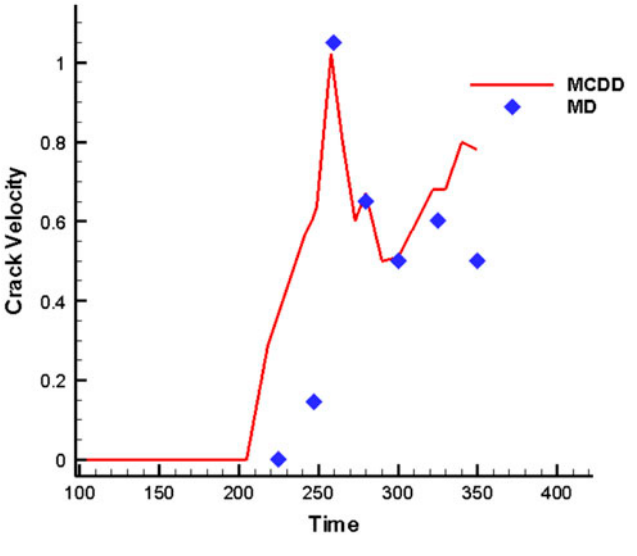

Figure 22. (colour online) Crack speed comparison between MCDD and MD simulations.

6.3. *Special numerical techniques in MCDD computations*

In the computations of two examples reported here, some special numerical techniques have been used in simulations, which are the integrated part of MCDD method; we shall discuss them in following.

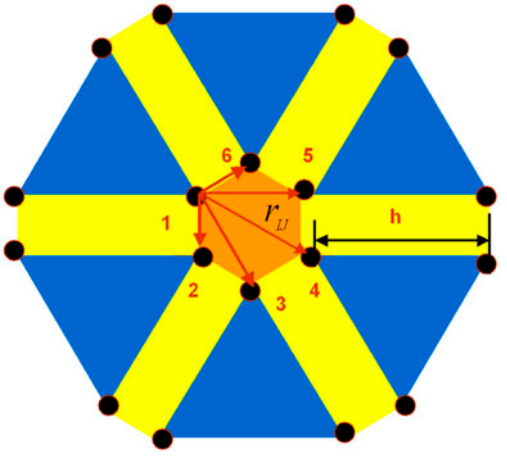

Figure 23. (colour online) Non-local interpolation scheme adopted in MCDD computations.

6.3.1. *Non-local interpolation of MCDD*

The proposed MCDD is a multiscale method that can seamlessly bridge the gap of several length scales. However when using MCDD to simulate atomistic scale problems, the partial differential equation-based local MCDD formation may reach to its limitation. To alleviate this shortcoming, we adopt the following non-local interpolation scheme in assemble final finite element dynamic equations. In the following, we use the two-dimensional hexagonal MCDD mesh as an example to illustrate the non-local interpolation technique.

Figure 23 shows a representative FEM node cluster distribution in a local region, which is shared by one second-order process zone element, six first-order process zone elements, and six bulk crystal elements. After the global internal force vector, $\mathbf{f}_I^{int}$, $I = 1, 2, \ldots 6$, have been assembled, we re-assemble them again based on the following non-local interpolation scheme,

$$\tilde{\mathbf{f}}_I = \frac{\sum_{J=1}^{6} \mathbf{f}_J w(r_{IJ})}{\sum_{J=1}^{6} w(r_{IJ})}, \quad I = 1, 2, \ldots, 6; \quad \text{where } w(x) = \exp(-x/r_0) H(2r_0 - x)$$

where $H(\cdot)$ is a Heaviside function, and r_0 is chosen as the one-third length of the first-order process zone element, h, i.e. $r_0 = h/7$; and $r_{IJ} = |\mathbf{r}_J - \mathbf{r}_I|$.

The MCDD dynamics equation then becomes,

$$\mathbf{M}\ddot{\mathbf{d}} + \tilde{\mathbf{f}}^{int}(\mathbf{d}) = \mathbf{f}^{ext}.$$

The non-local interpolation technique is crucial for both simulations of nano-indentation and crack propagation, because in both cases the Cauchy–Born rule-based constitutive relation will break down due to severe non-linear large deformation. Furthermore during

post failure regime even the higher order Cauchy–Born rule cannot accurately take into the non-local atomistic interaction in the crystal lattice as molecular dynamics does. The local FEM formulation has to be modified to mimic real material behaviours. From the practical computation standpoint, the non-local MCDD interpolation can effectively enforce the element impenetrability condition without invoking additional contact algorithm or any other ad hoc numerical treatments. Using the conventional Cauchy–Born rule-based approach simulating dislocation motion has its limitation, because that first the conventional finite element interpolation field do not provide any kinematic mechanism for dislocation or discontinuity formation; and second the system will soon loss its stability as demonstrated by [68]. If one does not update the support of an atom site, the shear failure caused debonding will soon cause the inter-element penetration. One way to address this problem is to enforce the inter-element impenetrability condition by either using classical contact algorithm or convexity requirements of process zone elements e.g. [24]. However, once we adopt the non-local FEM interpolation technique the element penetration phenomenon almost disappears.

6.3.2. *Quadrature in process zone elements*

In computations, the proposed process zone method is not a variant of element deletion algorithm, but an automatic element sliding and separation algorithm that is controlled by intrinsic material strength inside the process zone. Moreover, we hope to relate the numerical element sliding, separation, and disintegration with dislocation, fracture, and cavitation in microscale. To ensure such element sliding/separation/disintegration corresponding to real material failure phenomena, one has to make sure that there is no numerical mishandling. However, all the process zone elements used in MCDD are significantly smaller than the bulk crystal elements in at least one or more directions, which posts danger in shear-locking during numerical calculations. A systematic study on how to apply reduced integration/hour-glass mode control technique to correctly simulate process zone failure is still a work in progress. Here we report two reduced integration techniques that can be used as the hour-glass mode control measure. Taking 2D quadrilateral interphase element as an example, we have used the reduced integration technique to successfully to avoid hour-glass mode during fracture simulation. A two-point reduced integration scheme is illustrated in Figure 24. If the process zone is a thin layer fault, in actual computation, one may place all the quadrature points along the middle line the layer and it reduces the number of quadrature points by half.

6.3.3. *The width of the process zone element*

One open parameter in MCDD simulations is the width of the first-order process zone element, which essentially determines the sizes of all process zone elements. This is an important issue in MCDD simulations, and so far we have only had an incomplete study on it. For example, we show the load-deflection curves for nanoindentation under different interphase zone widthes in Figure 16. In this particular case, the MCDD result that fits best with MD result is the case when the width of the first-order process zone is chosen in the range of 1.25Å $\sim$ 1.75Å. It happens that the dislocations simulated in this example include the Shockley partial dislocation, whose Burgers vector is: $\mathbf{b} = \frac{\mathbf{a}}{6}\langle 1\,1\,2\rangle$ [26]. Consider the fact that the lattice constant for a single crystal copper (C_u) is: $a = 3.610\,\text{Å}$, and the real size of dislocation core in this case should be in the neighbourhood of $b = a/\sqrt{6} \sim 1.45\,\text{Å}$,

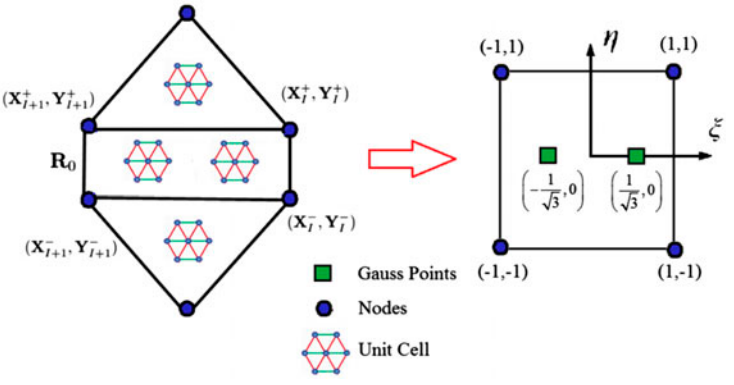

Figure 24. (colour online) Illustration of the reduced integration for quadrilateral interphase element.

which is almost the best choice of width for the first-order process zone. Since our simulation is a degenerated 2D simulation, further study is needed on how to choose the size of the process zone in 3D simulations.

7. Discussions

In this paper, we have presented a novel MCDD, and it has shown that MCDD can be used as a multiscale simulation tool to study defect mechanics in crystalline solids, and possibly its mesoscale statistical behaviours, i.e. crystalline plasticity.

The main novelties of MCDD are four:

- MCDD employs the DLPZ tessellation to represent or partition crystalline lattice space, and DLPZ tiling is a novel representation of both microstructure of crystalline solids and the microstructure of defects, which has not been explored before. In fact, the DLPZ solid is a homotopy of the original crystal lattice structure. However, the philosophy in MCDD is completely new: the DLPZ model is a representation or combination of both the crystalline solid and the embedded defects under the "same roof" rather than a perfect lattice complex without defects. This philosophy is also reflected how crystalline material fails, which we believe is a change of paradigm in computational materials science as well as defect mechanics.
- MCDD is based on the hypothesis that crystal defects will always (automatically) initiate inside the non-linear process zone, which is a fact observed in many experiments;
- MCDD employs an atomistic-informed higher order strain gradient formulation to construct constitutive relations for different order process zones, which have several distinct advantages: (1) providing both mathematical and physical regularization to ill-posed boundary value problems in the Cauchy–Born continuum, (2) providing physical and statistical links among different defects and (3) providing an approximation or a bridge between local continuum theory and discrete atomic theory and
- MCDD employs a non-local FEA interpolation technique that may take into account microscale non-local atomistic interaction with minimum effort and prevent element penetration.

Based on the preliminary results of MCDD simulations, we would like to make the following comments:

(1) We can construct 3D DLPZ solid for both BCC and FCC crystalline solids in both two-dimensional meshes as well as three-dimensional meshes. In fact, such construction of process zone tessellation is not unique, and this shall be further discussed in a separated paper;
(2) The key to a successful multiscale method is its ability to capture the non-local interaction at different scales while not using much computational resource as that of first principle-based methods. To accomplish this goal, in this work, we have done two things: First we adopt an atomistic-informed constitutive modelling, and second we adopt the high order strain gradient approach; The higher strain gradient approach not only confines non-linear deformation inside the process zone, but also makes them weak links in the homogeneous crystalline solid that allows automatically initiation of defects and defect evolution without the need of remeshing or re-construction of FEA interpolation field. In this regard, MCDD acts more or less like a cohesive zone model (CZM) [64], except it does not need to impose the ad hoc interface cohesive law, which creates a host of problems such as inability to deal with mixed-mode fracture, inconsistency between interface cohesive law and bulk constitutive relation etc.;
(3) We would like to point out that a main reason why MCDD works is because that the strain gradient theory is a special non-local theory in essence, and the relation between strain gradient theory and non-local theory has been articulated by several authors e.g. [4] and [65]; and in this work we actually devise a non-local FEA interpolation that can directly take into account the non-local effect in a local formulation, and
(4) By using MCDD, we can capture dislocation motion and crack propagation at the fine scale. It is true that MCDD has a prescribed superlattice process zone tiling, which can only cover a subset of the real lattice slip planes. Therefore, in this sense, MCDD is tiling- or mesh-dependent. However, the MCDD mesh dependence is different from the mesh-sensitive that the conventional cohesive zone method has, because the MCDD mesh dependence can be alleviated by successive mesh refinement, whereas in CZM method, the mesh dependence is intrinsic, and it will not disappear or alleviate after the mesh refinement (see [18]).

As any modelling method has its own limitation, MCDD has some issues too. In the following, we shall briefly discuss some important aspects of them:

- In applications of MCDD, additional information is needed in determining size or width of the process zone. Physically, almost all the defects have finite size, these include grain boundaries, phase boundaries, persistent slip bands (PSB), twin boundaries, etc., and they range from angstrom Å to micron size – that is the physical basis for the proposed MCDD method. By simulating defects as what they are in real physical world rather than as the idealized low-dimensional models, MCDD may achieve both computational efficiency and accuracy. However, in order to achieve atomistic resolution, MCDD may become more expensive than molecular simulation at atomistic scale. On the other hand, the success of superlattice process

zone tiling depends on the following scaling hypothesis that the defect evolution is self-similar within certain range of spatial scale, which is strong assumption;

- The MCDD formulation reported here does not contain temperature and heat dissipation or conduction, and it may only works for the case of 0° K temperature. However, a preliminary work for finite temperature process zone model has been reported by the present authors [39], which indicates that the extension of MCDD to finite temperature is feasible;
- In this paper, we only show how to construct DLPZ tessellation for BCC and FCC lattices, which are both monatomic and centrosymmetric crystal structures. We have yet to show how to construct the DLPZ tessellation for non-centrosymmetric/polyatomic structures, e.g. silicon, diamond, polarizable ionic crystals, which is a work in progress. Moreover, the atoms in polyatomic structure crystals, can undergo relative translations, so that the usual Cauchy–Born rule may not be applicable. To solve this problem, a correction to the Cauchy–Born rule for inner displacements has been proposed by several authors e.g. [15,37,57]. This type of MCDD formulations and simulations will be reported in a separated paper.
- The two numerical examples presented in this paper are all done in the setting of single crystal solids. MCDD can be readily modified and extended to simulate defect dynamics in polycrystalline solids that have grain boundaries, phase boundaries, persistent slip bands, etc. In fact, in a recent paper, we have simulated fracture in a polycrystalline solids by only using the 0th-order and the first-order process zone elements [46].

Acknowledgements

Dr. Lisheng Liu of Wuhan University of Science and Technology (China) had participated in the early phase of this research, and we benefited from many discussions with him. We would like to thank an anonymous reviewer for his comments and suggestions.

References

[1] F.F. Abraham, J.Q. Broughton, N. Bernstein and E. Kaxiras, Europhys. Lett. 44 (1998) p.783.
[2] R.J. Amodeo and N.M. Ghoniem, Phys. Rev. B 41 (1990) p.6958.
[3] M.P. Ariza and M. Oritiz, Arch. Ration. Mech. Anal. 178 (2005) p.149.
[4] Z. Bažant and M. Jirasek, ASCE J. Eng. Mech. 128 (2002) p.1119.
[5] T. Belytschko, *An overview of semidiscretization and time integration procedure*, in *Computational Methods for Transient Analysis*, T. Belytschko and T.J.R. Hughes, eds., North-Holland, Amsterdam, 1983, p.1.
[6] A. Björner, M. Las Vergnas, B. Sturmfels, N. White and G.M. Ziegler, *Oriented Matroids. Vol. 46, Encyclopedia of Mathematics*, Cambridge University Press, Cambridge, 1993.
[7] V.A. Blatov, Crystallogr. Rev. 10 (2004) p.249.
[8] V.V. Bulatov and W. Cai, *Computer Simulations of Dislocations*, Oxford University Press, Oxford, 2006.
[9] W. Cai, V.V. Bulatov, J.-P. Chang, J. Li and S. Yip, *Dislocation core effects on mobility*, in *Dislocations in Solids*, Vol. 12, Ch. 64, F.R.N. Nabarro and J.P. Hirth eds., Elsevier, Amsterdam, 2004, p.1. ISBN 044451483X.
[10] Y. Chen and J.D. Lee, Philos. Mag. 85 (2005) p.4095.

[11] Y. Chen, J. Chem. Phys. 124 (2006) Article No. 054113.
[12] J.D. Clayton, D.L. McDowell and D.J. Bammann, Int. J. Eng. Sci. 42 (2004) p.427.
[13] J.D. Clayton and P.W. Chung, J. Mech. Phys. Solids 54 (2006) p.1604.
[14] J.D. Clayton, Int. J. Solids Struct. 42 (2005) p.4613.
[15] J.D. Clayton, *Nonlinear Mechanics of Crystals*, Springer, Dordrecht, 2011.
[16] J.H. Conway and H. Burgiel, *The Symmetries of Things*, A.K. Peters, Wellesky, MA, 2008. ISBN 978-1-56881-220-5.
[17] B. Devincre and M. Condat, Acta Metall. Mater. 40 (1992) p.2629.
[18] M.L. Falk, A. Needleman, and J.R. Rice, J. Phys. IV France. 11 (2001) p.43.
[19] W. Fischer, E. Koch, and E. Hellner, Neues Jahrb. Mineral. Monatsh., 5 (1971) p.227.
[20] W. Fischer, H. Burzlaff, E. Hellner and J.D.H. Donnay, *Space Groups and Lattice Complexes. Natl Bur. Stand. (US) Monogr. No. 134*, National Bureau of Standards, Washington, 1973.
[21] W. Fischer and E. Koch, Z. Kristallogr. 150 (1979) p.245.
[22] H. Gao and P. Klein, J. Mech. Phys. Solids 46 (1998) p.187.
[23] N.M. Ghoniem, S.-H. Tong and L.Z. Sun, Phys. Rev. B 61 (2000) p.913.
[24] M. He and S. Li, Comput. Mech. 49 (2012) p.337.
[25] E. Hellner, Acta Crystallogr. 19 (1965) p.703.
[26] J.P. Hirth and J. Lothe, *Theory of Dislocations*, Krieger Publishing Co., Malabar, Florida, 1992. ISBN 0894646176.
[27] B.L. Holian and R. Ravelo, Phys. Rev. B 51 (1995) p.11275.
[28] M.F. Horstemeyer, M.I. Baskes, V.C. Prantil and J. Philliber, Modell. Simul. Mater. Sci. Eng. 11 (2003) p.265.
[29] T.J.R. Hughes, *The Finite Element Method: Linear Static and Dynamic Finite Element Analysis*, Prentice Hall, Englewood Cliffs, 1987.
[30] C.L. Kelchner, S.J. Plimpton and J.C. Hamilton, Phys. Rev. B 58 (1998) p.11085.
[31] E. Koch and W. Fischer, Acta Crystallogr. A 41 (1985) p.421–426.
[32] E. Koch and W. Fischer, Z. Kristallogr. 211 (1996) p.251–253.
[33] S. Li, X. Liu, A. Agrawal and A.C. To, Phys. Rev. B 74 (2006) Article No. 045418.
[34] S. Li and G. Wang, *Introduction to Micromechanics and Nanomechanics*, World Scientific, Singapore, 2008.
[35] S. Li, X. Zeng, B. Ren, J. Qian, J. Zhang and A.J. Jha, Comput. Methods Appl. Mech. Eng. 229–232 (2012) p.87. doi:10.1016/j.cma.2012.03.023
[36] X. Liu, S. Li and N. Sheng, Comput: Mech. 42 (2008) p.543.
[37] X. Liu, J. Gu, Y. Shen, J. Li and C. Chen, Acta Mater. 58 (2010) p.510.
[38] L. Liu and S. Li, *A multiscale crystal defect dynamics and its applications*, in *Multiscale Simulations and Mechanics of Biological Materials*, S. Li and D. Qing, eds., John Wiley & Sons, Chichester, West Sussex, 2012, p.43.
[39] L. Liu and S. Li, J. Eng. Mater. Technol. 134 (2012) Article No. 031014.
[40] R.E. Miller and E.B. Tadmor, J. Comput. Aided Mater. Des. 9 (2002) p.203.
[41] D.L. McDowell and G.B. Olson, Math. Stat. Sci. Model. Simul. 68 (2009) p.207.
[42] D.L. McDowell, Int. J. Plast. 26 (2010) pp.1280–1309.
[43] D.L. McDowell, JOM J. Miner. Met. Mater. Soc. 9 (2007) p.21.
[44] Y. Mishin, M.J. Mehl, D.A. Papaconstantopoulos, A.F. Voter and J.D. Kress, Phys. Rev. B. 63 (2001) p.224106.
[45] F. Nabarro, Adv. Phys. 1 (1952) p.269.
[46] J. Qian, and S. Li, ASME J. Eng. Mater. Technol. 133 (2011) p.011010.
[47] H.S. Park, E.G. Karpov, W.K. Liu and P.A. Klein, Philos. Mag. 85 (2005) p.79.
[48] R. Peierls, Proc. R. Soc. London 52 (1940) p.34.
[49] B. Ren and S. Li, Int. J. Numer. Methods Eng. 93 (2012) p.989.
[50] J.R. Rice, Mech. Mater. 6 (1987) p.317.
[51] R. Sauer and S. Li, Int. J. Numer. Methods Eng. 71 (2007) p.931.

[52] J. Schiøtz and K.W. Jacobsen, Science 301 (2003) p.1357.
[53] M. Senechal, *Quasicrystals and Geometry*, Cambridge University Press, Cambridge, UK, 1995.
[54] Y. Sun and K.M. Liew, Int. J. Numer. Methods Eng. 75 (2008) p.1238.
[55] R. Sunyk and P. Steinmann, Int. J. Solids Struct. 40 (2002) p.6877.
[56] E.B. Tadmor, M. Ortiz and R. Phillips, Philos. Mag. A62 (1996) p.1529.
[57] E.B. Tadmor and R.E. Miller, *Modeling Materials*, Cambridge University Press, Cambridge, 2011.
[58] G.I. Taylor, J. Inst. Met. 62 (1938) p.307.
[59] E.L. Wachspress, *A Rational Basis for Function Approximation. Vol. 228, Lecture Notes in Mathematics*, Springer, New York, 1971.
[60] G.J. Wagner and W.K. Liu, J. Comput. Phys. 190 (2003) p.249.
[61] J.B. Wang, X. Guo, H.W. Zhang, L. Wang and J.B. Liao, Phys. Rev. B. 73 (2006) p.115428.
[62] L. Xiong, G. Tucker, D.L. McDowell and Y. Chen, J. Mech. Phys. Solids 59 (2011) p.160.
[63] L. Xiong, Q. Deng, G. Tucker, D.L. McDowell and Y. Chen, Int. J. Plast. 38 (2012) p.86.
[64] X.-P. Xu and A. Needleman, J. Mech. Phys. Solids 42 (1994) p.1397.
[65] D. Yi, T.-C. Wang and Z. Xiao, Acta Mech. 212 (2010) p.51.
[66] X.W. Zeng and S. Li, Comput. Methods Appl. Mech. Eng. 199 (2010) p.547.
[67] Y. Zhong and T. Zhu, Comput. Methods Appl. Mech. Eng. 197 (2008) p.3174.
[68] T. Zhu, J. Li, K.J. van Vliet, S. Ogaraf, S. Yip and S. Suresha, J. Mech. Phys. Solids 52 (2004) p.691.